NASA
Technical
Paper
2412
C.2
May 1985

Total Energy-Rate Feedback for Automatic Glide-Slope Tracking During Wind-Shear Penetration

Christine M. Belcastro
and Aaron J. Ostroff

NASA

Total Energy-Rate Feedback for Automatic Glide-Slope Tracking During Wind-Shear Penetration

Christine M. Belcastro
and Aaron J. Ostroff

Langley Research Center
Hampton, Virginia

CONTENTS

SUMMARY

As a result of a study conducted by the Federal Aviation Administration in 1977 and a report published in 1983 by the National Research Council, low-altitude wind shear has become recognized as an infrequent but significant hazard to all aircraft during terminal-area operations. A sensor has been developed for measuring the time rate of change of the specific total energy of an airplane with respect to the air mass, and the sensor was tested and evaluated on a De Havilland DHC-6 Twin Otter airplane and also on the Transport Systems Research Vehicle (TSRV) B-737 airplane. Since total energy rate has been shown to be useful in wind-shear detection and in basic longitudinal stability and control studies, this sensor may be applicable to the wind-shear problem.

This paper presents a control system (both with and without energy-rate feedback) designed for the approach to landing of the TSRV B-737 through a severe-wind-shear and gust environment to evaluate the application of the total energy-rate sensor to wind-shear penetration during the landing phase of flight. A plant-system model is developed which incorporates wind-shear dynamics equations with the airplane equations of motion, thus allowing the control systems to be analyzed under various wind-shear conditions. The control systems are designed by using modern control theory and are formulated by using the proportional-integral-filter/command-generator tracking (PIF/CGT) control-law configuration integrated with optimal-output feedback. The feedback designs are analyzed with frequency-domain control-theory techniques for the design case with no wind and also for an off-design case with wind shear. Control-system performance is evaluated by using a complete nonlinear simulation of the airplane in combination with a severe-wind-shear and gust data package. This performance evaluation is concerned with control-system stabililty and regulation capability only - operational performance aspects, such as 100-ft decision height criteria and touchdown dispersion, are not considered. The analysis and simulation results indicate very similar stability and performance characteristics for the two designs. This outcome may be due to the availability and accuracy of the measurements that were used in this study. Energy-rate feedback may be beneficial on commercial transports that are not equipped with highly accurate measurement systems (e.g., inertial navigation systems) which are capable of providing all the necessary information or on commuter and general aviation aircraft, which have fewer available measurements for use in automatic control systems.

INTRODUCTION

Wind shear (or wind variability) is characterized by wind changes that depend on both distance and time. It can therefore be thought of as a local variation of wind velocity with respect to distance which occurs at some particular time. The magnitude and relative direction of a wind shear are quantified by dividing the velocity difference at two points by the distance between them, and this quantity is usually referred to as the wind-shear gradient.

Low-altitude wind shear results from thunderstorms and other convective clouds. It is recognized as an infrequent but significant hazard to all aircraft, from small general aviation airplanes to larger jet transports, during the take-off and the approach or landing phases of flight. A 1977 Federal Aviation Administration (FAA)

study (ref. 1) reported on aircraft accidents or incidents related to low-altitude wind shear occurring from 1964 to 1975. During this period, 25 cases involving transport airplanes were identified in which low-altitude wind shear was a possible cause of accidents during either the take-off (2 cases) or the approach or landing (23 cases). The most disastrous and well-known of these cases - in fact, the case that motivated the FAA study - was the 1975 landing accident at John F. Kennedy International Airport, which resulted in 112 fatalities. A later report under the auspices of the National Research Council (ref. 2) identified 27 cases related to low-altitude wind shear during the years 1964 to 1982. Four of the original twenty-five cases were eliminated as wind-shear-related accidents or incidents, but 6 new cases were identified for the time period 1976 to 1982, including the 1982 take-off accident at New Orleans International Airport which involved 153 fatalities.

Reference 2 lists 19 recommendations for reducing the flight hazards posed by low-altitude wind shear. Portions of two of the six recommendations listed under the section entitled "Aircraft Performance and Operations" are pertinent to the research presented in this paper. The following excerpts are from these recommendations:

Wind-Shear Effects on Flight Characteristics

The FAA should sponsor analytical and simulator investigations to determine the wind shear penetration and recovery capabilities of transport aircraft, based on various onboard detection, guidance, and control systems.

Guidance and Control Aids

Onboard sensors and guidance aids should be evaluated in a systematic manner to determine their merits for future development and for possible retrofit in existing aircraft. These include flight director modifications, ground speed/ airspeed flight mangement systems, vertical-acceleration sensors, and energy-rate sensors.

When an aircraft encounters a wind shear, changes occur in the wind-velocity components along each of the axes of motion of the airplane. Longitudinal wind shears run along the fuselage of the aircraft and are generally referred to as head-wind or tailwind shears depending on the direction. Vertical wind shears result from updrafts and downdrafts, which occur along the vertical axis of the aircraft. Longi-tudinal and vertical wind shears can add energy to or subtract energy from an air-craft because they affect the aircraft speed and altitude (i.e., its kinetic and potential energy, respectively) (ref. 2). These shears therefore have a major effect on the aircraft phugoid motion, which is characterized by constant total energy with a continual exchange between the kinetic and potential energy components. Further-more, certain wind-shear conditions can be shown to actually drive the phugoid mode to instability. Since total energy is the sum of kinetic and potential energy, its time rate of change with respect to the air mass reflects changes in altitude and airspeed due to wind-velocity changes. Thus, if total energy rate can be measured, information relating to wind shear will be available. Also, a measurement that pro-vides relatively fast information concerning wind shear, such as total energy rate, is particularly desirable over measurements that depend on the slow response of large airplanes.

Total energy rate has been used previously in research applications for wind-shear detection (ref. 3) and also for a basic piloted longitudinal stability and control study (ref. 4). In addition, a relatively simple and inexpensive total energy-rate sensor has been developed for measuring the time rate of change of the

2

specific energy (energy per unit weight) of an aircraft with respect to the air mass (refs. 5 to 9). The sensor system, consisting of a pressure-measuring probe in combination with an in-line acoustic filter and an altitude-rate transducer, was previously evaluated on both a De Havilland DHC-6 Twin Otter airplane (ref. 10) and on the Transport Systems Research Vehicle (TSRV) B-737 airplane at the NASA Langley Research Center (ref. 11). Both studies indicated a possible application of the sensor to the wind-shear problem and particularly to the automatic control of an airplane on final approach. Also, since this sensor is simple and relatively inexpensive, it is a good candidate to be retrofit on existing aircraft.

The purpose of this study is to determine the results of incorporating the energy-rate sensor into an automatic longitudinal control system for the approach to landing of a transport airplane in a severe-wind-shear and gust environment. Including gusts (or turbulence) with wind shear contributes to flight hazards and increases the chances of an accident (ref. 2). A system model is developed which incorporates the signal from the total energy-rate sensor (including sensor dynamics) into the airplane longitudinal equations of motion, and a control system is designed and analyzed both with and without the energy-rate measurement. In order to account for wind disturbances in the control-system design and analysis, wind-velocity equations representative of a linearly varying wind shear are incorporated into the system model, and wind-gust components are added as forcing functions. The control structure selected for the design presented in this paper is the proportional-integral-filter/command-generator tracking (PIF/CGT) (ref. 12) control-law formulation combined with optimal-output feedback.

The feedback designs are analyzed with frequency-domain control-theory techniques, whereas control-system performance is evaluated with time-history plots from a complete nonlinear simulation of the airplane combined with a severe-wind-shear and gust data package developed by SRI International. This data package includes a reconstruction of the hazardous wind-shear environment that occurred during the Kennedy airport landing accident, and this profile is used in the evaluation. This study is concerned with control-system stability and control regulation capability when subjected to a particularly hazardous wind-shear and gust environment. Operational performance aspects, such as 100-ft decision height criteria and touchdown dispersion, are important but were not considered in this research.

This paper presents a description of the PIF/CGT control-law structure with output feedback, the development of the design model, and a summary of the design, analysis, and simulation results. It is shown that the control-system concepts presented herein result in acceptable designs from the standpoint of stability and control regulation, with or without use of the total energy-rate sensor, and that inclusion of the sensor is not particularly advantageous. This outcome may, however, be due to the availability and accuracy of the measurements that were used in this study. Energy-rate feedback may be an advantage on commercial transports that are not equipped with highly accurate measurement systems, or on commuter and general aviation aircraft, which typically have fewer available measurements for use in automatic control.

DESIGN MODEL DEVELOPMENT

In order to evaluate the application of the total energy-rate sensor to the wind-shear problem, a longitudinal control law was developed for the approach to landing of an airplane through wind shear. The control structure selected for the design was the proportional-integral-filter/command-generator tracking (PIF/CGT)

discrete control-law formulation (ref. 12) combined with optimal-output feedback (ref. 13). This section provides a brief description of the control structure followed by the models required for the design.

The PIF formulation is a linear feedback control structure that allows the feedback of proportional and integrated states and that incorporates a control command filter to accommodate computational delay and to provide high-frequency-noise suppression. Proportional plus integral feedback provides partial trim accommodation in that the trim for the integrated states can be maintained while the proportional states go to new trims. The control command filter is implemented through the use of commanded control rates combined with proportional control-position/command feedback. The use of output feedback in the design precludes the necessity of estimating states so that only measurable aircraft parameters need be included in the output, and sensor, actuator, and engine dynamics can be accounted for in the state model. The PIF feedback design model is therefore comprised of a linear state (perturbation) model which incorporates plant, control, and integrator states in the state vector and uses control rates as commands. The output vector consists of selected measurable aircraft parameters in addition to the control and integrator states. The feedback gains are computed for the discrete system model in order to obtain a direct digital design.

The CGT formulation (ref. 14) provides a means of incorporating command-generating and tracking capabilities into the control-system design through the use of feedforward control gains. The feedforward design is implemented independently of the feedback design and requires a system design model in addition to a linear command model for the system to track. The system design model consists of the plant-state model used in the PIF design with the integrator states as its output, and the command model is formulated such that its output also corresponds to the integrator states. This construction enables the commands to these states to be tracked with type 1 system properties, thus enhancing the trim accommodation aspect of the design provided by the integrator states.

The PIF/CGT feedback and feedforward structures are combined in an incremental form so that the flight equations can be expressed in terms of total quantities rather than perturbations. This precludes the necessity of storing trim values. A summary of the equations involved in the PIF formulation, in the optimal-output feedback design, in the command generator for the feedforward design, and in the integration of these structures for flight implementation are presented in appendix A.

The TSRV B-737 airplane was selected for the design of this study for several reasons. First, computer programs were available in-house for determining the linear-perturbation model for some nominal flight condition (ref. 15) and also for performing a full nonlinear simulation of the airplane dynamic behavior in the presence of sensor noise and external disturbances such as wind shear. Second, the energy-rate sensor system had already been installed, calibrated, and evaluated on this airplane in a previous study (ref. 11), which yielded a fairly accurate second-order dynamic model approximation to use in the design. Also, this airplane, with the sensors already installed, could be used for flight tests, if indicated. The PIF augmented feedback-design model, including the plant-, control-, and integrator-state models, is now presented, followed by the command model used in the feedforward design.

The continuous plant-, control-, and integrator-state models required for the feedback design are presented first, followed by the PIF augmented design model.

Plant-state model.- The linearized continuous plant-state model combines the longitudinal aircraft states with those required for modeling the total energy-rate sensor (including sensor dynamics). Wind equations are also incorporated into the plant model so that wind disturbances can be accounted for in the control-system design and analysis. Other states included in this model represent altitude and engine dynamics. Appropriate output parameters were selected to be fed back to the controls. The plant-state model is summarized below, and all variables (unless otherwise noted) represent perturbations:

$$\dot{X} = AX + BU + B_w W \tag{1}$$

$$Y_X = H_X X \tag{2}$$

where

$$X = \begin{bmatrix} u, & w, & q, & \theta, & u_w, & w_w, & \dot{h}_{e,f}, & \dot{h}_{e,t}, & X_{th}, & h \end{bmatrix}^T \tag{3}$$

$$U = \begin{bmatrix} \delta_e, & \delta_{th} \end{bmatrix}^T \tag{4}$$

$$W = \begin{bmatrix} u_{w,g}, & w_{w,g} \end{bmatrix}^T \tag{5}$$

$$Y_X = \begin{bmatrix} V_a, & q, & \theta, & h, & \dot{h}, & \dot{h}_{e,t} \end{bmatrix}^T \tag{6}$$

The aircraft longitudinal states are given by u, w, q, and θ in equation (3). These represent, respectively, the longitudinal- and vertical-body-axis inertial velocity components, the pitch rate, and the pitch attitude. The longitudinal aircraft controls include elevator and throttle positions, and these are represented as δ_e and δ_{th} in equation (4). The linearized aerodynamic coefficients, needed for the A and B matrices of equation (1), were obtained from the computer program described in reference 15 for the flight condition listed in table I.

The next two states shown in equation (3) represent the longitudinal and vertical wind-velocity components u_w and w_w, expressed in the positive longitudinal and vertical directions of the body axes. These terms were included as states in the design model so the control law could be designed and analyzed for wind-shear disturbances. A linearized state wind model was therefore derived for incorporation with the airframe dynamic model. The wind model describes a wind-shear velocity for which the horizontal and vertical components vary linearly with respect to altitude. (Wind-velocity dependence on along-track position was not accounted for in this model, but it could easily be incorporated into the model for future studies.) Wind

5

velocities are obtained by integrating horizontal and vertical wind accelerations. Since the optimal-output feedback algorithm requires a strictly stable model, however, the wind-model equations used in the design represent a low-pass-filter approximation to this integration with poles located slightly into the left half-plane. The poles were subsequently placed back at the origin to represent a true integration for the analysis. This wind-shear model was patterned after one that was presented in reference 16, and a complete derivation is provided in appendix B.

Wind gusts are incorporated into the plant-state model as an additional forcing function, which is represented as W in equation (1). As defined in equation (5), W is a two-element vector containing the longitudinal and vertical wind-gust components. The wind-gust disturbance matrix B_w relates these components to the aircraft states through the same relationships as the aircraft velocity components (ref. 17). This wind-gust vector was added to the design model so that wind gusts could be incorporated into the optimal-output feedback design.

The next two states that appear in equation (3), $\dot{h}_{e,f}$ and $\dot{h}_{e,t}$, represent the second-order dynamic model of the energy-rate sensor. The model consists of a linearized expression for the specific total energy rate of the airplane $\dot{h}_e$ passed through a second-order low-pass filter with appropriate time constants (ref. 11) to model the energy-rate sensor dynamics. Appendix C contains a complete derivation of the linearized energy-rate equation, given by equation (C19), and the linear state model used for the sensor dynamics, given by equation (C20).

The engine-dynamics state X_{th} was modeled as a first-order lag with a cutoff frequency set equal to 0.75 rad/sec, which is the numerical mean of the cutoff frequencies associated with the engine response during acceleration and deceleration. This value was used so the average engine response between its two operational modes would be reflected in the design.

The altitude state h was modeled with the equation for altitude rate given in equation (C15) of appendix C, since potential energy rate per unit weight is equivalent to altitude rate by definition.

The output variables selected for the design are defined in equation (6). These include airspeed V_a, pitch rate q, pitch attitude θ, altitude h, altitude rate $\dot{h}$, and total energy rate $\dot{h}_{e,t}$. Only measurable aircraft quantities were included as outputs in the design model. The elements of the A, B, B_w, and H_X matrices of equations (1) and (2) are defined in appendix D.

Control-state model.- The control-state model required for the control command filter is formulated for the control-rate equation by

$$\dot{U} = V \tag{7}$$

where

$$V = \begin{bmatrix} \dot{\delta}_e, & \dot{\delta}_{th} \end{bmatrix}^T \tag{8}$$

<u>Integrator-state model</u>.- The states that were integrated in the PIF design model were altitude and airspeed. Altitude was integrated with the plant altitude state, and airspeed was integrated with the coefficients defined in equations (D9) to (D13) of appendix D. The integrator-state model can be written as

$$\dot{Z} = A_Z X + B_Z U \tag{9}$$

where

$$Z = \left[\int h, \int V_a \right]^T \tag{10}$$

and the matrix elements of A_Z and B_Z are defined in appendix D.

<u>Augmented PIF-state model</u>.- The complete augmented-feedback-design model was obtained by combining the plant-, control-, and integrator-state models developed in the preceding three sections. This model is summarized here as follows:

$$
\begin{bmatrix} \dot{X} \\ \dot{U} \\ \dot{Z} \end{bmatrix}
=
\begin{bmatrix} A & B & 0 \\ 0 & 0 & 0 \\ A_Z & B_Z & 0 \end{bmatrix}
\begin{bmatrix} X \\ U \\ Z \end{bmatrix}
+
\begin{bmatrix} 0 \\ I \\ 0 \end{bmatrix} V
+
\begin{bmatrix} B_W \\ 0 \\ 0 \end{bmatrix} W
\tag{11}
$$

$$
\begin{bmatrix} Y_X \\ Y_U \\ Y_Z \end{bmatrix}
=
\begin{bmatrix} H_X & 0 & 0 \\ 0 & H_U & 0 \\ 0 & 0 & H_Z \end{bmatrix}
\begin{bmatrix} X \\ U \\ Z \end{bmatrix}
\tag{12}
$$

where

$$Y_U = \left[\delta_e, \delta_{th} \right]^T \tag{13}$$

$$Y_Z = \left[\int h, \int V_a \right]^T \tag{14}$$

The terms H_U and H_Z of equation (12) are two-dimensional identity matrices, which enable the control-position commands and integrated states to be fed back to the controls. The above continuous state model was then discretized for a sampling period of 0.1 sec using the ORACLS computer program (ref. 18) as described in the "PIF Formulation" section of appendix A.

Command Model for Feedforward Control Design

The linear discrete command model that was used for the feedforward control design contained one state and two outputs for commanding altitude and airspeed (the same aircraft states being integrated) and is given by

$$[h_m]_{k+1} = [1] \; [h_m]_k + [\Delta T \quad 0] \begin{bmatrix} \dot{h}_c \\ \\ V_{a,c} \end{bmatrix}_k \tag{15}$$

$$\begin{bmatrix} h_m \\ \\ V_{a,m} \end{bmatrix}_k = \begin{bmatrix} 1 \\ \\ 0 \end{bmatrix} [h_m]_k + \begin{bmatrix} 0 & 0 \\ \\ 0 & 1 \end{bmatrix} \begin{bmatrix} \dot{h}_c \\ \\ V_{a,c} \end{bmatrix}_k \tag{16}$$

where $\dot{h}_c$ and $V_{a,c}$ are the desired-altitude-rate and desired-airspeed inputs to the command model, and h_m and $V_{a,m}$ are the commanded altitude and airspeed model outputs to be followed. The discrete sampling period ΔT is equal to 0.1 sec.

CONTROL-SYSTEM DESIGN AND ANALYSIS

The model described in the preceding section was used to design the PIF/CGT control system for the approach to landing of the TSRV B-737 airplane. This section presents the feedback designs, with and without energy-rate feedback, that were obtained with the output feedback-design program (ref. 13), an analysis of each design from the computer programs of reference 19 and an in-house singular-value package, the feedforward design which was obtained in the manner discussed in reference 14, and an evaluation using a nonlinear simulation program of the TSRV B-737 airplane.

Feedback Design and Analysis With Total Energy-Rate Feedback

In order to compute the feedback gains via the optimal-output feedback-design program (ref. 13), an initial set of weights for the states and controls and an initial set of process- and measurement-noise uncertainties had to be assigned so that the discrete weighting and covariance matrices required by the output feedback algorithm could be obtained. (See appendix A.) The state and control weights were obtained by computing the inverse square of the maximum allowable deviation for each state and control. These deviations were selected based on the corresponding trim values. The process-noise uncertainties were obtained by selecting reasonable values with respect to trim (based on engineering judgement) for an initial condition error for each of the states and controls and by assigning uncertainty values for severe wind gusts. Measurement-noise uncertainties were selected to represent typical noise spectra for the sensors that are onboard the TSRV B-737 airplane.

The initial set of discrete weighting and covariance matrices was then input to the optimal-output feedback program along with the discrete system matrices (for the no-wind-shear case) in order to obtain an initial set of feedback gains. These gains

were then evaluated with frequency-domain analysis techniques and nonlinear simulation time histories. Weightings or uncertainties or both were modified to improve system stability and performance characteristics, and a new set of gains was computed and evaluated. This process continued until a final set of gains was obtained. A listing of all the weightings and uncertainties used in the final design is presented in table II, and the corresponding feedback gains are listed in table III.

In order to analyze each design, the closed-loop eigenvalues were computed, and the gain and phase margins were obtained using Bode and singular-value plots. The Bode plots were computed with the loop broken at the actuator inputs (rather than at the rate commands) for each control separately while the other control loop remained closed. Only the input corresponding to the opened control response was considered. The singular-value plots were computed with both control loops broken at the actuator inputs for additive and multiplicative disturbances. This analysis was performed for the design case with no wind shear and also for a selected case with severe wind shear, both of which were run with the small wind poles (referred to previously) set to zero to represent the true wind-shear integration. The gradients for the off-design case were estimated from a reconstruction of the Kennedy airport wind-shear environment (referred to in the "Introduction"), which was developed as a software package by SRI International and is shown in figure 1. This profile was generated for the nominal flight path of the airplane under control of the above design, with flare being initiated at 42 ft above the runway. The altitude and along-track position shown in the figure are plotted with respect to the airplane center of gravity (c.g.), and the zero point on the x_{cg} scale is located at the end of the runway before touchdown. The gradients were calculated for specific time periods based on a nominal sink rate of 11 ft/sec. As shown in figure 1, the most severe gradients of the horizontal-wind-shear component occurred approximately from 46 to 54 sec and from 74 to 83 sec, and those for the vertical-wind-shear component occurred from 56 to 60 sec, from 64 to 74 sec, and from 74 to 86 sec. These gradients were then paired together to represent three realistic but severe environments. The open-loop eigenvalues were computed for each, and the worst case was selected for the off-design analysis. Table IV lists the open-loop short-period and phugoid poles for each of these wind-shear environments, and table V summarizes the analysis results for the final-design and off-design cases. An increasing headwind (tailwind) is represented as ↑HW (↑TW), and an increasing updraft (downdraft) is represented as ↑UD (↑DD).

Since the phugoid poles are the most unstable for the third wind-shear condition listed in table IV, this was selected as the off-design worst case condition for the feedback analysis. The eigenvalues given in table V are listed with the phugoid poles first, the short-period poles second, followed by the remaining poles of the system listed in order of increasing value. In the open-loop eigenvalues for the design case, −1.13 and −2.40 represent respectively the acoustic-filter and transducer dynamics of the energy-rate sensor, −0.75 represents the engine-dynamics state, two of the poles at the origin represent the wind states (since the small wind poles were set to zero to represent a true wind-shear integration for the analysis), and the five remaining poles at the origin represent the altitude state, the elevator control state, the throttle control state, and the two integrator states for altitude and airspeed. The unstable pole listed under the closed-loop eigenvalues for the off-design case is due to the wind states (which are uncontrollable) and is not indicative of an unstable aircraft system. The gain and phase margins (GM and PM) computed in the Bode analysis represent the stability margins of the system when one control loop is opened. The gain and phase margins computed in the singular value analysis, however, represent the guaranteed stability margins of the system for either additive or multiplicative disturbances when both control loops are open.

Feedback Design and Analysis Without Energy-Rate Feedback

The feedback system presented in the preceding section was redesigned without energy-rate feedback with the same weights and uncertainties as those given in table II. The values associated with the energy-rate signal, however, were modified such that energy rate could be removed from the system without reducing the order of the model. These modifications included reducing the weighting on the two energy-rate states to zero, decreasing the uncertainty associated with these states to 0.001, and increasing the uncertainty associated with the energy-rate measurement to 100. All these changes tended to force the gains assigned to the energy-rate signal toward zero, which effectively removed it from the feedback loop. Table VI lists the gains obtained for the redesign without energy-rate feedback, and the corresponding analysis is summarized in table VII for both the design and the off-design case.

The open-loop eigenvalues are not repeated in table VII because they are the same as those listed in table V. The analysis results indicate some differences in the closed-loop eigenvalues and stability margins for the two designs, but most of these differences are small. For the off-design case, feeding back energy rate appears to move the phugoid poles slightly farther into the left half-plane. In addition, the phase margins for the energy-rate-feedback design are slightly better, particularly when the throttle loop is open. These results suggest that the energy-rate signal may provide added phugoid-mode stability in wind shear, but the amount may be negligible in this application. Removing the energy-rate signal, alternatively, seems to provide a little more damping to the phugoid and short-period modes for both the design and the off-design case.

Feedforward Design and Analysis

The feedforward gains were computed as in reference 14 for the altitude and airspeed command model defined in equations (15) and (16). Since the state model and the states to be integrated were not altered for the two feedback designs (with and without energy-rate feedback), the feedforward design was the same for both systems. The feedforward gains are therefore summarized for either system as follows:

$$A_{11} = \begin{bmatrix} 0 \\ 0 \\ 0 \\ 0 \\ 0 \\ 0 \\ 0 \\ 0 \\ 0 \\ 1.0 \end{bmatrix} \qquad (17)$$

$$A_{12} = \begin{bmatrix} 0.00049 & 1.0100 \\ -0.02100 & -0.41500 \\ 0 & 0 \\ 0.00460 & -0.00180 \\ 0 & 0 \\ 0 & 0 \\ 1.00000 & 0 \\ 1.00000 & 0 \\ 0.62800 & 0.09940 \\ 0 & 0 \end{bmatrix} \tag{18}$$

$$A_{21} = \begin{bmatrix} 0 \\ 0 \end{bmatrix} \tag{19}$$

$$A_{22} = \begin{bmatrix} 0.1170 & 0.1010 \\ 0.6280 & 0.0994 \end{bmatrix} \tag{20}$$

In order to analyze the feedforward control system, a nonlinear simulation of the TSRV B-737 airplane was used with implementation of altitude and airspeed commands which were computed with the command model of equations (15) and (16) for the altitude rate and airspeed input commands shown in figure 2. The altitude-rate and airspeed command-model inputs were computed from a constant desired-altitude acceleration and airspeed rate, respectively. Figure 3 shows the results of the nonlinear simulation of the TSRV B-737 following these commands in an environment which is uncorrupted by either noise or wind. Since no wind was introduced into the system, the ground-speed plot of figure 3 shows the airplane tracking the velocity (or airspeed) command. The altitude-rate response of the airplane is also following the desired-altitude rate. The plots of airspeed error ΔV_a and altitude error Δh, which indicate the difference between the actual output and the commanded value, show that the airplane altitude and airspeed followed the command-model outputs except during the transitions, with airspeed having the slower response. The altitude measurement used in this simulation run was radar altitude. This signal, however, is generally replaced on the airplane by a third-order complementary-filter estimate (ref. 20), which is computed with respect to the runway coordinates. Figure 4 shows the same command-following simulation run with radar altitude replaced by this altitude estimate from a complementary filter. During flight, this filter is initialized prior to engaging the control system so that initialization transients can damp out. This takes approximately 60 to 80 sec. In this simulation, however, the complementary filter was not initialized prior to engaging the control system. Therefore, in the figure, it is clear that the altitude response has been degraded due to these initialization transients introduced by the complementary filter, particularly since the filter dynamics were not included in the design model. This effect is evident during the first 60 sec of the altitude-error plot, which is consistent with the time

constants associated with the complementary-filter response. The simulations presented in the next section all use this complementary-filter estimate for altitude rather than radar altitude. Therefore, additional error in the Δh plots will be present, particularly during the first 60 sec, that should not occur in actual practice.

CONTROL-SYSTEM PERFORMANCE

In order to evaluate control-system stability and control regulation capability under hazardous wind-shear and gust conditions, the control-system designs were implemented (using the flight equations presented in appendix A) in a nonlinear simulation of the TSRV B-737 which was used in conjunction with the SRI International wind-shear and gust data package. Operational performance aspects, such as 100-ft decision height criteria and touchdown dispersion, were not considered in this evaluation. The simulations began with the trimmed airplane located on a 3° glide slope at a mean-sea-level altitude of approximately 1300 ft. The airplane was commanded to descend down the glide slope at constant airspeed until the airplane initiated flare at 42 ft above the runway. During flare, the aircraft was commanded to follow an exponential path with a constant deceleration of 3 ft/sec^2. The simulations ended when touchdown occurred. The airplane equations of motion were computed every 0.05 sec, and the control commands were updated every 0.10 sec for a desired altitude along the glide slope and a desired airspeed. A slower sampling rate was sufficient for implementing this control system because it is a direct digital-control-law design. This is a major advantage of performing a direct digital design over discretizing a continuous control-law design. The 0.10-sec time increment was selected for this application based on previous experience in implementing a digital control system on the TSRV B-737 (ref. 21). All the simulation results discussed in this section were for the Kennedy airport wind-shear reconstruction shown in figure 1 combined with a corresponding gust package that contains root-mean-square (rms) gust intensities up to 13 ft/sec (ref. 22). The lateral-wind-velocity component was set to zero, however, to reduce lateral effects. Figure 5 shows a time-history plot of this wind-shear and gust environment as it was used in the simulations, although time varies slightly for each run due to varying ground speed. All the design runs presented used the altitude estimate from the third-order complementary filter rather than the radar altitude, and measurement noise which was representative of the sensors onboard the airplane was incorporated into the simulations. Position and rate limits for the control-surface servos and actuators were also included. Lateral control was implemented within the simulation for maintaining the wings level and the desired heading, but there was no closed-loop control for localizer tracking. This section presents the simulation results for the control-system design both with and without energy-rate feedback (figs. 6 to 9), followed by the performance of the TSRV B-737 instrument landing system (ILS) autoland system in this environment as a comparison (fig. 10). In order to provide information regarding aircraft altitude in these results (figs. 6 to 10), the point at which the airplane is approximately 100 ft above the runway is indicated along the time scale of the figures. A brief discussion of robustness is then presented for several off-nominal cases in which basic airplane parameters such as c.g. location, weight, and airspeed were varied. Slight variations in these parameters had little effect on control-system performance, so inclusion of these effects as separate figures was not warranted. However, in order to present these effects in this paper, the results presented in figures 6 to 9 are those for which the airplane c.g. was slightly different from the design. The glide-slope angle was then increased to 5° and these results for each design are presented in figures 11 and 12. All these plots represent total aircraft quantities except where noted.

Performance of the Design With Energy-Rate Feedback

Nonlinear simulation results for the control-system design with total energy-rate feedback are shown in figures 6 and 7. The first case (fig. 6) contains airspeed in the measurement set (see eq. (6)), whereas the second case (fig. 7) contains the velocity V, which distributes the velocity feedback gains between airspeed V_a and ground speed V_g according to the following implementation:

$$V_k = (1 - c)V_{a,k} + c\, V_{g,k} \tag{21}$$

where

$$c = 0 \qquad (V_{a,m} < V_g) \tag{22}$$

is for total airspeed control

$$c = \frac{V_{a,m} - V_g}{V_\ell} \qquad (V_g < V_{a,m} < V_g + V_\ell) \tag{23}$$

is for linear distribution between airspeed and ground speed, and

$$c = 1 \qquad (V_{a,m} > V_g + V_\ell) \tag{24}$$

is for total ground-speed control.

In equations (22) to (24), $V_{a,m}$ is the airspeed generated by the CGT model, and V_ℓ is determined by the allowable lower limit on ground speed. This modification does not alter the validity of the design analyses since the total velocity gains remain unchanged. In most cases, V_a will have the larger component of feedback gain, and for the case of a tailwind, all the feedback gain is applied to regulation of V_a. The limit of 50 ft/sec was selected for V_ℓ to prevent stall in case of a sudden wind change from a headwind to a tailwind.

From figure 6, the worst altitude error Δh is -65 ft, with one-third of this error caused by the complementary-filter initialization transients. The airspeed data show tight tracking through the peak headwind of approximately 60 ft/sec, which occurred at around 70 sec into the run. During the time period of 85 to 110 sec, however, ΔV_a decreases by 70 ft/sec, V_g drops to 130 ft/sec, α increases to 17°, θ increases to 24°, and δ_{th} reaches saturation (60°). It is interesting to note that this time period corresponds to a decreasing headwind and a decreasing downdraft, as shown in figure 5, and can be related to the increasing tailwind and increasing updraft condition evaluated in the "Control-System Design and Analysis" section and found to induce phugoid-mode instability. Although the simulation does not indicate that stall occurred, the aircraft may actually reach stall under these

conditions due to several factors that were not accounted for in the simulation. For example, slight asymmetries that exist in the wings of the aircraft were not modeled in the simulation. Also, lateral effects due to winds and closed-loop localizer tracking were not included. Either of these factors could cause a wing to stall under the conditions of low V_a and high α shown in figure 6, resulting in the aircraft reaching stall.

The implementation of the control system was therefore modified as previously discussed to limit decreases in V_g while maintaining enough V_a control to prevent stall during severe shifts from headwind to tailwind shears. These results are presented in figure 7. In contrast to figure 6, this figure shows that V_a is allowed to increase during the large headwind, with the subsequent decrease being much smaller than in the previous case. In fact, V_a never decreases very much below the commanded value. Furthermore, δ_{th} just touches saturation, θ remains relatively low during the severe-wind-shear time period, and α remains relatively constant throughout the entire approach and landing. The total run time is approximately 5 sec shorter because of better regulation of V_g.

Operational aspects that were not addressed in this study include the 100-ft decision height criteria for continuing the approach or implementing a go-around (this includes maintaining an adequate thrust reserve for effecting a go-around, if necessary) and touchdown conditions for an acceptable landing. These operational aspects could probably be improved by using additional implementation techniques similar to the one presented here and by gain scheduling. For example, an upper V_g limit was implemented in the same manner as the lower limit in an effort to reduce the high V_g at touchdown, and this proved to be effective in accomplishing the desired reduction. These results were not included in the figures, however, because they were preliminary in nature and additional modifications would still be required for an operationally acceptable touchdown, which was not an objective of this study.

Performance of the Design Without Energy-Rate Feedback

The same simulation results as those just presented for the design with energy-rate feedback are repeated in figures 8 and 9 for the redesign of the control system without energy-rate feedback. As shown in figure 8, removing the energy-rate measurement actually appears to slightly improve control regulation capability. The value ΔV_a is reduced to approximately -56 ft/sec, α is reduced to 15°, and θ is reduced to about 22°, while the maximum Δh error remains about the same. In addition, δ_e and δ_{th} activity is slightly reduced when the energy-rate signal is removed. The results shown in figure 9 also indicate a slight improvement in the control-regulation capability of the redesign without energy-rate feedback, although the differences between this figure and figure 7 are less pronounced than those between figure 8 and figure 6. The overall results for the two designs are very similar, however, and both sets of results indicate a dramatic improvement in the regulation capability of the implementations with distributed V_a and V_g control over those with V_a control only.

TSRV B-737 ILS Autoland-System Performance

The performance of the instrument landing system (ILS) autoland control system onboard the TSRV B-737 airplane (ref. 20) is presented in figure 10 as a baseline run for comparison. The initial conditions and trim values for this run are set equal to those which were used for the previous design runs. The ILS system is an analog

control law that is implemented digitally on the airplane flight-control computers at a rate of 20 times per second, and the simulation program has an equivalent implementation. Figure 10 shows that the ILS system is able to maintain acceptable stability and control regulation until the airplane encounters the decreasing-headwind/decreasing-downdraft condition mentioned previously. During this time period, ΔV_a decreases by 65 ft/sec, Δh decreases by 138 ft, α increases to 24°, θ increases to 30°, and δ_e reaches its lower saturation limit. The value of δ_{th} during this period touches 60°. The 24° limitation on α shown in figure 10 is imposed within the simulation because of the unavailability of aerodynamic data beyond this point. In actuality, α would continue to increase until the airplane reaches stall. The simulation indicates that the airplane may begin to stall during this period, but that altitude is recovered (and, in fact, reaches 256 ft above the glide slope) subsequent to δ_e saturating its upper limit. A definite stall condition probably would occur in reality, however, without the limitation on α. Also, wing asymmetries and lateral wind effects could also combine with this condition, as discussed previously, to cause stall during this period. Furthermore, if the decreasing-headwind/decreasing-downdraft condition had occurred any later in the run, the airplane probably would have impacted the ground even though a recovery may have been theoretically possible. The airplane lands in the simulation, however, and the large positive Δh error indicated at touchdown results from the glide slope extending beneath the runway beyond the glide-slope intercept point.

A comparison of the ILS results of figure 10 with those shown in figures 7 and 9 indicates that both designs are able to maintain much better control stability and regulation quality in this environment than the ILS system. During the same critical time period, the worst error occurs in θ, which increases to 11° and 10° respectively for figures 7 and 9, and δ_{th} just touches its 60° position limit. All other parameters, however, are held fairly constant throughout this period, and δ_e stays below 6.5° in figure 7 (design with energy-rate feedback) and below 4.7° in figure 9 (redesign without energy-rate feedback). Furthermore, even the design results presented in figures 6 and 8 for the initial implementation are preferable to those shown in figure 10 for the ILS system. This may be because of the optimal integrated elevator-throttle structure of these designs, combined with the ability to account for process noise, measurement noise, and control-position and rate saturation limits during the design process.

Robustness

A precursory evaluation of the control-system designs for robustness was obtained for three off-design cases by varying the c.g. location, weight, and airspeed of the aircraft and repeating the simulation runs with the previously described velocity gain distribution for each design. The off-design cases selected for this analysis are presented in the following table:

Case	c.g., percent MAC	Weight, lb	Airspeed, knots
1	10	85 000	135
2	20	85 000	125
3	30	75 000	119

The effect of this variation on the simulation results was not significant enough to warrant presenting these runs as separate figures. However, in order to include the effect of slight parameter variations on the performance of the control-system designs presented in this paper, the preceding simulation results shown in figures 6 to 9 are for off-design case 2 listed above, which represents a slightly off-nominal c.g. location. (The aircraft parameters for the design included a c.g. location at 25 percent MAC rather than at 20 percent MAC.) This off-design case was then repeated for each design with the glide-slope angle increased from 3° to 5°, and these results are presented in figures 11 and 12. It is shown in these figures that the pitch attitude and throttle activity are worse in these runs, but the general performance of both designs is very similar to the results presented in figures 7 and 9.

SUMMARY, CONCLUSIONS, AND RECOMMENDATIONS

A control system with and without energy-rate feedback has been developed for the approach to landing of the Transport Systems Research Vehicle (TSRV) B-737 airplane through a severe-wind-shear and gust environment to evaluate the application of a total energy-rate sensor to the wind-shear problem. The analysis and simulation results for the two designs can be summarized as follows:

1. A simple implementation technique for distributing the velocity feedback gains between airspeed and ground speed proved to be very effective in reducing pitch attitude, angle of attack, and throttle activity during severe-wind-shear and gust penetration while maintaining good airspeed and altitude control. This implementation technique does not alter the design or the validity of the analysis since the total feedback gains remain unchanged, but operational performance criteria may be affected.

2. The control-law design, both with and without total energy-rate feedback, demonstrated the capability of following both altitude and airspeed commands with zero steady-state error and of penetrating a severe-wind-shear and gust environment during the approach to landing.

3. Integrating the airplane and wind-shear dynamics as coupled differential equations indicated wind-shear conditions for which the airplane phugoid mode was unstable. This modeling approach allowed the control law to be analyzed for these unstable conditions.

4. Minor differences appeared in the analysis and simulation results of the control-law design with total energy-rate feedback compared with those of the control-law design without total energy-rate feedback, but none of these were of great significance.

5. The instrument landing system (ILS) autoland system onboard the TSRV B-737 airplane was much less effective in penetrating the severe-wind-shear and gust environment than were the control-law designs (with and without total energy-rate feedback) considered in this paper.

From these results, the following conclusions may be drawn:

1. The energy-rate sensor may be better applied to aircraft with a more limited and less accurate measurement field, such as for commercial transports that are not equipped with an inertial navigation system or for commuter and general aviation

aircraft, since the other measurements studied herein appear to provide all the necessary information.

2. The design concepts, control-law structure, and implementation techniques presented in this paper are applicable, with or without use of the energy-rate sensor, to the wind-shear problem, and these designs are much more effective in maintaining stability and control regulation during severe-wind-shear and gust penetration than conventional systems. This may be because of the optimal integrated multivariable structure of these designs and the ability to account for process noise, measurement noise, and control-position and rate saturation limits during the design process.

3. Incorporating wind-shear-dynamics equations with the airplane equations of motion for the plant design model is an effective means of providing control-system analysis capability for various wind-shear conditions.

Based on the results and conclusions of this study, the following recommendations are offered for future study:

1. A possible extension to this study would be to investigate the sensor for a reduced measurement field, such as for transports without the inertial navigation system or for a commuter or general aviation aircraft. The value of fast-response wind-related information provided by the total energy-rate sensor may be of greater importance there than in the application of this study.

2. The wind-shear model presented in this paper includes wind component acceleration as a function of altitude rate. This wind-shear model should be expanded to include wind component acceleration as a function of the longitudinal velocity of the airplane. The expanded model would allow a more thorough investigation of sensitive wind-shear conditions and control-system analysis under these wind-shear conditions.

3. Additional research should include operational design criteria, that is, maximum and minimum airspeed and ground-speed criteria, 100-ft decision height flight characteristics, and touchdown dispersion under various wind-shear and gust environments.

4. A further application of these concepts might be to develop a similar design for take-off.

NASA Langley Research Center
Hampton, VA 23665
January 18, 1985

APPENDIX A

CONTROL-LAW STRUCTURE

This appendix presents a summary of the PIF formulation, the output feedback equations, the CGT formulation, and the flight equations used in the design and evaluation of the control systems presented in this paper. All variables represent perturbation quantities unless otherwise noted.

PIF Formulation

The continuous-time design model using the PIF structure is given by the following:

$$\dot{\bar{X}} = \bar{A}\bar{X} + \bar{B}V + \bar{B}_w W \tag{A1}$$

$$\bar{Y} = \bar{H}\bar{X} + \bar{N} \tag{A2}$$

$$\bar{X} = \begin{bmatrix} x^T, & u^T, & z^T \end{bmatrix}^T \tag{A3}$$

$$\bar{Y} = \begin{bmatrix} Y_X^T, & Y_U^T, & Y_Z^T \end{bmatrix}^T \tag{A4}$$

$$\bar{A} = \begin{bmatrix} A & B & 0 \\ 0 & 0 & 0 \\ A_z & B_z & 0 \end{bmatrix} \tag{A5}$$

$$\bar{B} = \begin{bmatrix} 0 \\ I \\ 0 \end{bmatrix} \tag{A6}$$

$$\bar{B}_w = \begin{bmatrix} B_w \\ 0 \\ 0 \end{bmatrix} \tag{A7}$$

where

X	state vector for the plant
U	control position-command state vector
Z	integrator-state vector
V	control rate-command vector
W	wind-gust vector
$\bar{\mathbf{Y}}$	output vector
$\mathbf{Y_X}$	output vector for the plant states
$\mathbf{Y_U}$	output vector for the control states
$\mathbf{Y_Z}$	output vector for the integrated states
$\bar{\mathbf{N}}$	PIF output-noise vector
A,B	plant-state and control-state matrices
B_w	wind-gust disturbance matrix
$\bar{H}$	observation matrix
A_Z, B_Z	transmission matrices for the integrator states

The discrete form of the state equation given in equation (A1) can be obtained by using the ORACLS computer program (ref. 18). The discrete design model can be written as follows:

$$\bar{X}_{k+1} = \bar{F}\bar{X}_k + \bar{G}V_k + \bar{G}_w W_k \tag{A8}$$

$$\bar{Y}_k = \bar{H}\bar{X}_k + \bar{N}_k \tag{A9}$$

where $\bar{F}$, $\bar{G}$, and $\bar{G}_w$ are the discrete matrices corresponding to $\bar{A}$, $\bar{B}$, and $\bar{B}_w$ as obtained from ORACLS. However, several approximations to $\bar{F}$ and $\bar{G}$ are made in order to implement both a zero-order hold for the control-rate commands and an Euler discrete integration (ref. 12). The final form for $\bar{F}$ and $\bar{G}$, then, becomes

$$\bar{F} = \begin{bmatrix} F & G & 0 \\ 0 & I & 0 \\ \Delta T\ A_Z & \Delta T\ B_Z & I \end{bmatrix} \tag{A10}$$

19

$$\bar{G} = \begin{bmatrix} 0 \\ \Delta T \ I \\ 0 \end{bmatrix} \tag{A11}$$

where ΔT is the discrete sampling period and I represents appropriately dimensioned identity matrices.

Output Feedback Equations

A stochastic, discrete optimal-output feedback design program (ref. 12) was used to compute the feedback gains for the selected outputs of equation (A9). The continuous-time cost function J is given by

$$J = E \left\{ \int_0^\infty \bar{x}^T \bar{Q} \bar{x} + v^T \bar{R}_v v \ dt \right\} \tag{A12}$$

where $E\{\ \}$ is the expected value and $\bar{Q}$ is a diagonal state-weighting matrix with components given by

$$\bar{Q} = \text{diag} \left[Q_X, \ Q_U, \ Q_Z \right] \tag{A13}$$

where Q_X is the plant-state-weighting matrix, Q_U is the control-position command-state-weighting matrix, and Q_Z is the integrator-state-weighting matrix. The control-rate command-weighting matrix is represented by the diagonal matrix $\bar{R}_v$. All weightings described in the "Control-System Design and Analysis" section are inserted into equation (A12).

The equivalent discrete performance index, which is required in reference 13, is defined as

$$J = \lim_{N \to \infty} \frac{1}{N} E \left\{ \sum_{k=-1}^{N} \bar{x}_k^T \hat{Q} \bar{x}_k + 2 \bar{x}_k^T \hat{M} v_k + v_k^T \hat{R} v_k \right\} \tag{A14}$$

where $\hat{Q}$ and $\hat{R}$ are the discrete weighting matrices corresponding to $\bar{Q}$ and $\bar{R}_v$ as calculated with the sampling period ΔT using reference 18. The term $\hat{M}$ is the discrete cross-weighting matrix between states and controls.

The output feedback formulation also includes both plant process noise and measurement noise. Terms included in the plant process noise are randomly distributed

initial-condition errors, control-input random pseudonoise, and random wind-gust disturbances. The total discrete plant-process-noise covariance $\bar{W}$ is calculated as:

$$\bar{W} = \bar{F}\bar{X}_i\bar{F}^T + \int_0^{\Delta T}\left[e^{\bar{A}t}\left(\bar{B}\bar{V}_p\bar{B}^T + \bar{B}_w\bar{W}_g\bar{B}_w^T\right)e^{\bar{A}^Tt}\right]dt \tag{A15}$$

$$E\{\bar{x}_i\} = 0 \tag{A16a}$$

$$E\{\bar{x}_i\bar{x}_i^T\} = \bar{X}_i\delta_{ij} \tag{A16b}$$

$$E\{\bar{v}\} = 0 \tag{A17a}$$

$$E\{\bar{v}\bar{v}^T\} = \bar{V}_p\delta_{ij} \tag{A17b}$$

$$E\{\bar{w}\} = 0 \tag{A18a}$$

$$E\{\bar{w}\bar{w}^T\} = \bar{W}_g\delta_{ij} \tag{A18b}$$

where $\bar{X}_i$ is the initial-condition error covariance, $\bar{V}_p$ is the control-input process-noise covariance, $\bar{W}_g$ is the wind-gust process-noise covariance, and δ_{ij} is the Kronecker delta function. The terms $\bar{x}_i$, $\bar{v}$, and $\bar{w}$ contain respectively the state, control, and wind uncertainties described in the "Control System Design and Analysis" section of this paper. The integral term in equation (A15) is transformed to the discrete form using reference 18. The measurement-noise covariance $\bar{V}_m$ is calculated in a similar manner as follows:

$$E\{\bar{N}\} = 0 \tag{A19a}$$

$$E\{\bar{N}\bar{N}^T\} = \bar{V}_m\delta_{ij} \tag{A19b}$$

where $\bar{N}$ contains the measurement-noise uncertainties.

The optimal-feedback gains K are directly related to the output measurement as

$$V_k = K\bar{Y}_k \tag{A20}$$

with the corresponding closed-loop transition matrix $\bar{F}_{cl}$ given by

$$\bar{F}_{cl} = \bar{F} + \bar{G}K\bar{H} \qquad (A21)$$

CGT Formulation

The objective of command-generator tracking (CGT) is to cause selected outputs $Y_{z,k}$ of the airplane to optimally track the output $Y_{m,k}$ of a linearized command model by using feedforward control gains. The open-loop plant model can be written as

$$X_{k+1} = FX_k + GU_k \qquad (A22)$$

$$Y_{z,k} = A_z X_k + B_z U_k \qquad (A23)$$

and the linearized command is given by

$$X_{m,k+1} = F_m X_{m,k} + G_m U_{m,k+1} \qquad (A24)$$

$$Y_{m,k} = H_m X_{m,k} + D_m U_{m,k+1} \qquad (A25)$$

It should be noted that the output vector $Y_{z,k}$ in equation (A23) corresponds to the airplane states being integrated in equation (A8), and that the model outputs $Y_{m,k}$ in equation (A25) are the commanded values for these same states. The reason for using an advanced time step on the control is presented in reference 12. The feed-forward gains relate the model states X_m and model controls U_m to ideal star trajectory X^*, U^* as follows:

$$\begin{bmatrix} X^* \\ U^* \end{bmatrix}_k = \begin{bmatrix} A_{11} & A_{12} \\ A_{21} & A_{22} \end{bmatrix} \begin{bmatrix} X_{m,k} \\ U_{m,k+1} \end{bmatrix} \qquad (A26)$$

where each A_{ij} represents a constant feedforward gain matrix. The solution for the feedforward gains involves solving equation (A26) as follows:

$$\begin{bmatrix} A_{11} & A_{12} \\ A_{21} & A_{22} \end{bmatrix} = \begin{bmatrix} F-I & G \\ A_z & B_z \end{bmatrix}^{-1} \begin{bmatrix} A_{11}(F_m-I) & A_{11}G_m \\ H_m & D_m \end{bmatrix} \qquad (A27)$$

22

A method for solving equation (A27) and the derivations involved are presented in reference 14. (A more detailed derivation is presented in TIM No. 612-2 of The Analytic Sciences Corporation entitled "Command Generator Tracking - The Discrete Time Case"; this document is not widely available.)

Flight Equations

The CGT model is integrated into the feedback design by letting the perturbation model (eq. (A8)) represent the error between the plant perturbation states and controls and the star trajectory perturbation states and controls. If we use an incremental control-law form and rigorously substitute total quantities into the perturbation model (similar to ref. 12, which uses full-state feedback as opposed to the output feedback used in this paper), the flight equations become

$$\mathbf{E}_{T,k} = \bar{\mathbf{Y}}_{\mathbf{X},T,k} - \bar{\mathbf{H}}_{\mathbf{X}} A_{11} \mathbf{X}_{m,T,k} \tag{A28}$$

$$\mathbf{V}_{T,k} = (\mathbf{I} + \Delta T\, K\bar{\mathbf{H}}_{\mathbf{U}})\mathbf{V}_{T,k-1} + K(\mathbf{E}_{T,k} - \mathbf{E}_{T,k-1})$$

$$+ \Delta T\, K\bar{\mathbf{H}}_{\mathbf{Z}}(\mathbf{Y}_{\mathbf{Z},T,k-1} - \mathbf{Y}_{m,T,k-1}) + E_1(\mathbf{U}_{m,T,k+1} - \mathbf{U}_{m,T,k}) \tag{A29}$$

$$\mathbf{U}_{T,k+1} = \mathbf{U}_{T,k} + \Delta T\, \mathbf{V}_{T,k} \tag{A30}$$

where

$$\mathbf{Y}_{\mathbf{X},T,k} = \begin{bmatrix} \mathbf{Y}_{\mathbf{X},T,k}^T & 0^T & 0^T \end{bmatrix}^T \tag{A31}$$

$$\bar{\mathbf{H}} = \begin{bmatrix} \bar{\mathbf{H}}_{\mathbf{X}} & \bar{\mathbf{H}}_{\mathbf{U}} & \bar{\mathbf{H}}_{\mathbf{Z}} \end{bmatrix} \tag{A32}$$

$$E_1 = -K\left(\bar{\mathbf{H}}_{\mathbf{X}} A_{12} + \bar{\mathbf{H}}_{\mathbf{U}} A_{22} + \bar{\mathbf{H}}_{\mathbf{Z}} P_A\right) \tag{A33}$$

$$P_A = -P_{\mathbf{ZZ}}^{-1}\left(P_{\mathbf{XZ}}^T A_{12} + P_{\mathbf{UZ}}^T A_{22}\right) \tag{A34}$$

where $P_{\mathbf{XZ}}^T$, $P_{\mathbf{UZ}}^T$, and $P_{\mathbf{ZZ}}$ represent the rows of the optimal-output feedback solution matrix of equation (A14) that correspond to the integrator states. The subscript T's in the above equations indicate these are total quantities.

WIND-MODEL DERIVATION

This appendix presents a complete derivation of the linear wind-shear states which were incorporated into the control-law design model presented in this paper.

The wind-velocity vector in the inertial Earth-fixed reference frame is given by

$$\mathbf{V}_{w,E} = U_{w,E}\mathbf{x} + W_{w,E}\mathbf{z} \tag{B1}$$

where $\mathbf{x}$ and $\mathbf{z}$ are unit vectors. This vector is then rotated to the body axes by using the following transformation:

$$\begin{bmatrix} U_w \\ W_w \end{bmatrix}_b = \begin{bmatrix} \cos\theta & -\sin\theta \\ \sin\theta & \cos\theta \end{bmatrix} \begin{bmatrix} U_w \\ W_w \end{bmatrix}_E \tag{B2}$$

The resulting body-axis expression for wind velocity is

$$\mathbf{V}_w = (U_{w,E}\cos\theta - W_{w,E}\sin\theta)\mathbf{x}_b$$

$$+ (U_{w,E}\sin\theta + W_{w,E}\cos\theta)\mathbf{z}_b \tag{B3}$$

Differentiating the $\mathbf{x}_b$ and $\mathbf{z}_b$ components of equation (B3) yields

$$\dot{U}_w = \dot{U}_{w,E}\cos\theta - U_{w,E}\dot{\theta}\sin\theta - \dot{W}_{w,E}\sin\theta - W_{w,E}\dot{\theta}\cos\theta \tag{B4}$$

$$\dot{W}_w = \dot{U}_{w,E}\sin\theta + U_{w,E}\dot{\theta}\cos\theta + \dot{W}_{w,E}\cos\theta - W_{w,E}\dot{\theta}\sin\theta \tag{B5}$$

Substituting

$$\dot{\theta} = Q \tag{B6}$$

for pitch rate in equations (B4) and (B5) yields

$$\dot{U}_w = \dot{U}_{w,E} \cos \theta - QU_{w,E} \sin \theta - \dot{W}_{w,E} \sin \theta - QW_{w,E} \cos \theta$$

$$= \dot{U}_{w,E} \cos \theta - \dot{W}_{w,E} \sin \theta - W_w Q \tag{B7}$$

$$\dot{W}_w = \dot{U}_{w,E} \sin \theta + QU_{w,E} \cos \theta + \dot{W}_{w,E} \cos \theta - QW_{w,E} \sin \theta$$

$$= \dot{U}_{w,E} \sin \theta + \dot{W}_{w,E} \cos \theta + U_w Q \tag{B8}$$

The following expressions for $U_{w,E}$ and $W_{w,E}$ can now be obtained for a hypothetical linear wind shear that varies with respect to decreasing altitude:

$$U_{w,E} = u_{w,E,o} + U_z Z_E = u_{w,E,o} + u_{w,E} \tag{B9}$$

$$W_{w,E} = w_{w,E,o} + W_z Z_E = w_{w,E,o} + w_{w,E} \tag{B10}$$

where

$u_{w,E,o}$ some nominal constant horizontal wind velocity

$w_{w,E,o}$ some nominal constant vertical wind velocity

$u_{w,E}$ horizontal wind-velocity perturbation due to wind shear

$w_{w,E}$ vertical wind-velocity perturbation due to wind shear

U_z horizontal wind-shear gradient, (ft/sec)/ft

W_z vertical wind-shear gradient, (ft/sec)/ft

Z_E aircraft altitude, positive down (-H)

Differentiating equations (B9) and (B10) yields

$$\dot{U}_{w,E} = U_z \dot{Z}_E = \dot{u}_{w,E} \tag{B11}$$

$$\dot{W}_{w,E} = W_z \dot{Z}_E = \dot{w}_{w,E} \tag{B12}$$

where $\dot{u}_{w,E}$ and $\dot{w}_{w,E}$ represent the total wind perturbations from the nominal wind velocities $u_{w,E,o}$ and $w_{w,E,o}$.

25

Equations (B11) and (B12) can be related to the airplane dynamics by defining $\dot{Z}_E$ to be the sink rate of the airplane along the glide slope (i.e., for a frozen wind field). The sink-rate equation as a function of the airplane longitudinal- and vertical-body-axis velocity components is given by

$$\dot{Z}_E = -U \sin \theta + W \cos \theta \tag{B13}$$

Substituting equation (B13) into equations (B11) and (B12) yields

$$\dot{U}_{w,E} = -U_Z (U \sin \theta - W \cos \theta) \tag{B14}$$

$$\dot{W}_{w,E} = -W_Z (U \sin \theta - W \cos \theta) \tag{B15}$$

The complete nonlinear expressions for the longitudinal- and vertical-body-axis wind-acceleration components can now be determined by substituting equations (B14) and (B15) into equations (B7) and (B8):

$$\dot{U}_w = -U_Z (U \sin \theta - W \cos \theta) \cos \theta + W_Z (U \sin \theta - W \cos \theta) \sin \theta - W_w Q \tag{B16}$$

$$\dot{W}_w = -U_Z (U \sin \theta - W \cos \theta) \sin \theta - W_Z (U \sin \theta - W \cos \theta) \cos \theta + U_w Q \tag{B17}$$

The linearized expressions for the wind-acceleration components can be obtained by performing a perturbation expansion on equations (B16) and (B17) with the following substitutions:

$$U = u_o + u \tag{B18}$$

$$W = w_o + w \tag{B19}$$

$$\theta = \theta_o + \theta \tag{B20}$$

$$Q = q_o + q \tag{B21}$$

$$W_w = w_{w,o} + w_w \tag{B22}$$

$$U_w = u_{w,o} + u_w \tag{B23}$$

26

where u_o, w_o, θ_o, and q_o are the nominal trimmed aircraft parameters, and u, w, θ, and q represent perturbations. Substituting equations (B18) to (B23) into equations (B16) and (B17), inserting appropriate trigonometric identities, expanding, and collecting terms yields the final form of the wind-model equations:

$$\dot{u}_w = \left[-U_z(0.5 \sin 2\theta_o) + W_z\left(\sin^2\theta_o\right)\right]u + \left[U_z\left(\cos^2\theta_o\right) - W_z(0.5 \sin 2\theta_o)\right]w + (-w_{w,o})q$$

$$+ \left[-(U_zu_o + W_zw_o) \cos 2\theta_o - (U_zw_o - W_zu_o) \sin 2\theta_o\right]\theta + (-q_o)w_w \qquad (B24)$$

$$\dot{w}_w = \left[-U_z\left(\sin^2\theta_o\right) - W_z(0.5 \sin 2\theta_o)\right]u + \left[U_z(0.5 \sin 2\theta_o) + W_z\left(\cos^2\theta_o\right)\right]w + (u_{w,o})q$$

$$+ \left[-(U_zu_o + W_zw_o) \sin 2\theta_o + (U_zw_o - W_zw_o) \cos 2\theta_o\right]\theta + (q_o)u_w \qquad (B25)$$

$$\dot{u}_{w,o} = -U_z\left[u_o(0.5 \sin 2\theta_o) - w_o\left(\cos^2\theta_o\right)\right] - W_z\left[w_o(0.5 \sin 2\theta_o) - u_o\left(\sin^2\theta_o\right)\right]$$

$$- q_ow_{w,o} \qquad (B26)$$

$$\dot{w}_{w,o} = U_z\left[w_o(0.5 \sin 2\theta_o) - u_o\left(\sin^2\theta_o\right)\right] - W_z\left[u_o(0.5 \sin 2\theta_o) - w_o\left(\cos^2\theta_o\right)\right]$$

$$+ q_ou_{w,o} \qquad (B27)$$

Equations (B24) and (B25) represent the wind-shear perturbations from the desired flight path, and equations (B26) and (B27) represent the nominal wind-shear perturbations from the constant wind velocities $u_{w,o}$ and $w_{w,o}$ along the desired flight path. The terms $u_{w,o}$ and $w_{w,o}$ are obtained by rotating the nominal constant wind-velocity components in the Earth-fixed inertial frame $u_{w,E,o}$ and $w_{w,E,o}$ to their equivalent body-axis components with equation (B2). The sign conventions implicit in the above equations are summarized as follows:

$u_{w,E,o} > 0$ for constant tailwind
$w_{w,E,o} > 0$ for constant downdraft
$U_z > 0$ for increasing tailwind with descent
$W_z > 0$ for increasing downdraft with descent

Equations (B24) and (B25) are the linearized wind-state-model equations, and each wind-velocity component is obtainable through a pure integration of these acceleration components. The wind-model equations used in the design, however, represent a low-pass-filter approximation to this integration (because of a restriction in the

27

control-law algorithm requiring a strictly stable system), and these equations are given below:

$$\dot{u}_W = \left[-U_z(0.5 \sin 2\theta_o) + W_z(\sin^2\theta_o)\right]u + \left[U_z(\cos^2\theta_o) - W_z(0.5 \sin 2\theta_o)\right]w$$

$$+ (-w_{w,o})q + \left[-(U_z u_o + W_z w_o) \cos 2\theta_o - (U_z w_o - W_z u_o) \sin 2\theta_o\right]\theta$$

$$+ (-u_{w,\omega})u_W + (-q_o)w_W \tag{B28}$$

$$\dot{w}_W = \left[-U_z(\sin^2\theta_o) - W_z(0.5 \sin 2\theta_o)\right]u + \left[U_z(0.5 \sin 2\theta_o) + W_z(\cos^2\theta_o)\right]w$$

$$+ (u_{w,o})q + \left[-(U_z u_o + W_z w_o) \sin 2\theta_o + (U_z w_o - W_z u_o) \cos 2\theta_o\right]\theta$$

$$+ (q_o)u_W + (-w_{w,\omega})w_W \tag{B29}$$

where

u_o nominal inertial velocity component of the airplane in the positive X-direction of the body axes

w_o nominal inertial velocity component of the airplane in the positive Z-direction of the body axes

$u_{w,o}$ nominal component of wind velocity in the positive longitudinal direction of the body axes

$w_{w,o}$ nominal component of wind velocity in the positive vertical direction of the body axes

U_z horizontal wind-shear gradient with respect to decreasing altitude

W_z vertical wind-shear gradient with respect to decreasing altitude

$\dot{u}_{w,o}$ nominal wind-shear acceleration in the positive X-direction of the body axes

$\dot{w}_{w,o}$ nominal wind-shear acceleration in the positive Z-direction of the body axes

$u_{w,\omega}$ small low-pass cutoff frequency for the horizontal-body-axis wind-velocity component

$w_{w,\omega}$ small low-pass cutoff frequency for the vertical-body-axis wind-velocity component

The cutoff frequencies $u_{w,\omega}$ and $w_{w,\omega}$ were selected to be small with respect to wind spectra and the system bandwidth, so that the frequency response of the wind "filters" would approximate an integrator for those frequencies. This approximation

was incorporated into the design model, because the output feedback algorithm used in the design requires that the initial system be strictly stable. Hence, incorporation of the small low-pass-filter poles adequately approximated the integrations while allowing the eigenvalues associated with the wind states to be located slightly into the left half-plane rather than at the origin, thus meeting the stability requirement. These poles were subsequently set back at the origin for the control-system analysis.

TOTAL ENERGY-RATE MODEL DERIVATION

This appendix presents a complete derivation for the linear energy-rate equation used to represent the energy-rate sensor model presented in this paper. Total energy E_T can be expressed in terms of potential energy E_p and kinetic energy E_k as follows:

$$E_T = E_p + E_k = mgH + (1/2)mV_a^2 \tag{C1}$$

where H indicates total altitude. The total specific energy per unit weight, or energy height H_e, is obtained as

$$H_e = H + (1/2g)V_a^2 \tag{C2}$$

Differentiating equation (C2) yields the basic total energy-rate model used in the design:

$$\dot{H}_e = \dot{H} + (1/g)V_a\dot{V}_a \tag{C3}$$

where the first term represents the potential energy-rate component of the airplane and the second term represents the kinetic energy-rate component. Since the potential energy-rate component is simply the altitude rate, the body-axis equation can be expressed as

$$\dot{H}_{pe} = U \sin \theta - W \cos \theta \tag{C4}$$

Since the kinetic energy-rate component was found in reference 11 to measure the airspeed and airspeed-rate terms along the longitudinal direction of the body axes, the kinetic energy-rate component is written as

$$\dot{H}_{ke} = (1/g)V_{a,x}\,\dot{V}_{a,x} \tag{C5}$$

where

$$V_{a,x} = U - U_w \tag{C6}$$

$$\dot{V}_{a,x} = \dot{U} - \dot{U}_w \tag{C7}$$

30

Equation (C5) includes only the longitudinal-direction velocity and acceleration components because it was previously determined in reference 11 that this quantity provides a better representation of the total energy-rate sensor measurement. The term $\dot{U}$ in equation (C7) represents the airplane longitudinal acceleration and is a function of the airplane states and wind-velocity components in the longitudinal and vertical directions of the body axes.

Equations (C4) and (C5) can be linearized through a perturbation expansion with the following substitutions:

$$U = u_0 + u \tag{C8}$$

$$W = w_0 + w \tag{C9}$$

$$\Theta = \theta_0 + \theta \tag{C10}$$

$$V_{a,x} = V_{a,x,o} + v_{a,x} \tag{C11}$$

$$\dot{V}_{a,x} = \dot{V}_{a,x,o} + \dot{v}_{a,x} \tag{C12}$$

$$v_{a,x} = u - u_w \tag{C13}$$

$$\dot{v}_{a,x} = \dot{u} - \dot{u}_w \tag{C14}$$

Substituting equations (C8) to (C10) into equation (C4) yields the linearized potential energy-rate perturbation

$$\dot{h}_{pe} = u \sin \theta_0 - w \cos \theta_0 + (u_0 \cos \theta_0 + w_0 \sin \theta_0)\theta \tag{C15}$$

and substituting equations (C11) to (C14) into equation (C5) yields the linearized kinetic energy-rate perturbation

$$\dot{h}_{ke} = (\dot{V}_{a,x,o}/g)u - (\dot{V}_{a,x,o}/g)u_w + (V_{a,x,o}/g)\dot{u} - (V_{a,x,o}/g)\dot{u}_w \tag{C16}$$

where

$$V_{a,x,o} = u_0 - u_{w,o} \tag{C17}$$

$$\dot{V}_{a,x,o} = \dot{u}_0 - \dot{u}_{w,o} \tag{C18}$$

$$\dot{u} = a_{11}u + a_{12}w + a_{13}q + a_{14}\theta + a_{15}u_w + a_{16}w_w + b_{11}\delta_e + b_{12}\delta_{th} \tag{C19}$$

$$\dot{u}_w = w_{11}u + w_{12}w + w_{13}q + w_{14}\theta + w_{15}u_w + w_{16}w_w + \dot{u}_{w,o} \tag{C20}$$

Adding equations (C15) and (C16), collecting terms, and substituting equations (C19) and (C20) for the acceleration terms $\dot{u}$ and $\dot{u}_w$ yields the final form of the energy-rate equation required for the design presented in this paper:

$$\dot{h}_e = \left[\sin\theta_o + (\dot{V}_{a,x,o}/g) + (V_{a,x,o}/g)(a_{11} - w_{11})\right]u$$

$$+ \left[-\cos\theta_o + (V_{a,x,o}/g)(a_{12} - w_{12})\right]w + \left[(V_{a,x,o}/g)(a_{13} - w_{13})\right]q$$

$$+ \left[u_o\cos\theta_o + w_o\sin\theta_o + (V_{a,x,o}/g)(a_{14} - w_{14})\right]\theta$$

$$+ \left[-(\dot{V}_{a,x,o}/g) + (V_{a,x,o}/g)(a_{15} - w_{15})\right]u_w + \left[(V_{a,x,o}/g)(a_{16} - w_{16})\right]w_w$$

$$+ \left[(V_{a,x,o}/g)(b_{11})\right]\delta_e + \left[(V_{a,x,o}/g)(b_{12})\right]\delta_{th} \tag{C21}$$

where a_{11} to a_{16} and b_{11} and b_{12} represent the constant coefficient terms associated with the perturbed-airplane inertial acceleration $\dot{u}$ in the positive longitudinal direction of the body axes, and w_{11} to w_{16} represent the constant coefficient terms associated with the perturbed-wind acceleration $\dot{u}_w$ in the positive longitudinal direction of the body axes, derived in appendix B. The term u_o is the nominal body longitudinal inertial velocity component, θ_o is the nominal pitch attitude, and $u_{w,o}$ is the nominal wind-velocity component in the positive longitudinal direction of the body axes. The terms $V_{a,x,o}$ and $\dot{V}_{a,x,o}$ are the nominal longitudinal airspeed and longitudinal airspeed-rate components and g is the acceleration due to gravity. The term $\dot{u}_o$ is the nominal body longitudinal inertial acceleration component of the airplane, and $\dot{u}_{w,o}$ is the nominal wind-shear acceleration in the positive longitudinal direction of the body axes and is also derived in appendix B.

The energy-rate signal in equation (C21) was then passed through a second-order low-pass filter with appropriate time constants (ref. 11) in order to model the energy-rate sensor dynamics. This filter was modeled as follows:

$$\begin{bmatrix} \dot{X}_f \\ \dot{X}_t \end{bmatrix} = \begin{bmatrix} -\omega_f & 0 \\ \omega_t & -\omega_t \end{bmatrix} \begin{bmatrix} X_f \\ X_t \end{bmatrix} + \begin{bmatrix} \omega_f \\ 0 \end{bmatrix} \dot{h}_e \tag{C22}$$

where X_f and ω_f are the state and the cutoff frequency associated with the acoustic filter, and X_t and ω_t are the state and the cutoff frequency associated with the altitude-rate transducer. (From ref. 11, $\omega_f = 1.13$ rad/sec and $\omega_t = 2.40$ rad/sec.)

APPENDIX D

DESIGN MODEL DEFINITION

This appendix defines the matrix elements of the design model given by equations (11) and (12). These equations are repeated here for convenience:

$$
\begin{bmatrix} \dot{X} \\ \dot{U} \\ \dot{Z} \end{bmatrix} = \begin{bmatrix} A & B & 0 \\ 0 & 0 & 0 \\ A_z & B_z & 0 \end{bmatrix} \begin{bmatrix} X \\ U \\ Z \end{bmatrix} + \begin{bmatrix} 0 \\ I \\ 0 \end{bmatrix} V + \begin{bmatrix} B_w \\ 0 \\ 0 \end{bmatrix} W
$$

$$
\begin{bmatrix} Y_X \\ Y_U \\ Y_Z \end{bmatrix} = \begin{bmatrix} H_X & 0 & 0 \\ 0 & H_U & 0 \\ 0 & 0 & H_Z \end{bmatrix} \begin{bmatrix} X \\ U \\ Z \end{bmatrix}
$$

The matrices given in these equations are defined as follows:

$$
A = \begin{bmatrix}
a_{11} & a_{12} & a_{13} & a_{14} & -a_{11} & -a_{12} & 0 & 0 & K_e(b_{12}) & 0 \\
a_{21} & a_{22} & a_{23} & a_{24} & -a_{21} & -a_{22} & 0 & 0 & K_e(b_{22}) & 0 \\
a_{31} & a_{32} & a_{33} & a_{34} & -a_{31} & -a_{32} & 0 & 0 & K_e(b_{32}) & 0 \\
0 & 0 & 1 & 0 & 0 & 0 & 0 & 0 & 0 & 0 \\
w_{11} & w_{12} & w_{13} & w_{14} & w_{15} & w_{16} & 0 & 0 & 0 & 0 \\
w_{21} & w_{22} & w_{23} & w_{24} & w_{25} & w_{26} & 0 & 0 & 0 & 0 \\
k_1\omega_f & k_2\omega_f & k_3\omega_f & k_4\omega_f & k_5\omega_f & k_6\omega_f & -\omega_f & 0 & K_e\omega_f(p_2) & 0 \\
0 & 0 & 0 & 0 & 0 & 0 & \omega_t & -\omega_t & 0 & 0 \\
0 & 0 & 0 & 0 & 0 & 0 & 0 & 0 & -\omega_e & 0 \\
h_1 & h_2 & 0 & h_4 & 0 & 0 & 0 & 0 & 0 & 0
\end{bmatrix}
\qquad \text{(D1)}
$$

$$
B = \begin{bmatrix} b_{11} & 0 \\ b_{21} & 0 \\ b_{31} & 0 \\ 0 & 0 \\ 0 & 0 \\ 0 & 0 \\ \omega_f(p_1) & 0 \\ 0 & 0 \\ 0 & \omega_e \\ 0 & 0 \end{bmatrix}
\qquad (D2)
$$

$$
A_z = \begin{bmatrix} 0 & 0 & 0 & 0 & 0 & 0 & 0 & 0 & 0 & 1 \\ a_{z_{21}} & a_{z_{22}} & 0 & 0 & a_{z_{25}} & a_{z_{26}} & 0 & 0 & 0 & 0 \end{bmatrix}
\qquad (D3)
$$

$$
B_z = \begin{bmatrix} 0 & 0 \\ 0 & 0 \end{bmatrix}
\qquad (D4)
$$

$$
B_w = \begin{bmatrix} -a_{11} & -a_{12} \\ -a_{21} & -a_{22} \\ -a_{31} & -a_{32} \\ 0 & 0 \\ -a_{51} & -a_{52} \\ -a_{61} & -a_{62} \\ -a_{71} & -a_{72} \\ 0 & 0 \\ 0 & 0 \\ -a_{101} & -a_{102} \end{bmatrix}
\qquad (D5)
$$

34

$$
H_{\mathbf{X}} =
\begin{bmatrix}
a_{z_{21}} & a_{z_{22}} & 0 & 0 & a_{z_{25}} & a_{z_{26}} & 0 & 0 & 0 & 0 \\
0 & 0 & 1 & 0 & 0 & 0 & 0 & 0 & 0 & 0 \\
0 & 0 & 0 & 1 & 0 & 0 & 0 & 0 & 0 & 0 \\
0 & 0 & 0 & 0 & 0 & 0 & 0 & 0 & 0 & 1 \\
h_1 & h_2 & 0 & h_4 & 0 & 0 & 0 & 0 & 0 & 0 \\
0 & 0 & 0 & 0 & 0 & 0 & 0 & 1 & 0 & 0
\end{bmatrix}
\tag{D6}
$$

$$
H_{\mathbf{U}} =
\begin{bmatrix}
1 & 0 \\
0 & 1
\end{bmatrix}
\tag{D7}
$$

$$
H_{\mathbf{Z}} =
\begin{bmatrix}
1 & 0 \\
0 & 1
\end{bmatrix}
\tag{D8}
$$

where

$$
a_{z_{21}} = (u_o - u_{w,o})/V_{a,o}
\tag{D9}
$$

$$
a_{z_{22}} = (w_o - w_{w,o})/V_{a,o}
\tag{D10}
$$

$$
a_{z_{25}} = -a_{z_{21}}
\tag{D11}
$$

$$
a_{z_{26}} = -a_{z_{22}}
\tag{D12}
$$

$$
V_{a,o} = \left[(u_o - u_{w,o})^2 + (w_o - w_{w,o})^2\right]^{1/2}
\tag{D13}
$$

The K_e term is an engine constant that relates engine thrust to throttle position, and the value used for the TSRV B-737 was 596 lb/deg. The w_{1j} and w_{2j} terms in equation (D1) are the coefficient terms defined in equations (B22) and (B23), respectively. The k_j and p_j terms in equations (D1) and (D2) are the coefficient terms in equation (C19) of appendix C relating the plant states and controls, respectively, to total energy rate. The h_j terms in equations (D1) and (D6) are the coefficient terms for the altitude rate given in equation (C15). The $V_{a,o}$ term is the nominal total airspeed. The terms a_{ij} are linearized aerodynamic terms for the airplane.

35

REFERENCES

1. Shrager, Jack J.: The Analysis of National Transportation Safety Board Large Fixed-Wing Aircraft Accident/Incident Reports for the Potential Presence of Low-Level Wind Shear. FAA-RD-77-169, Dec. 1977. (Available from DTIC as AD A048 354.)

2. Comm. on Low-Altitude Wind Shear and Its Hazard to Aviation: Low-Altitude Wind Shear and Its Hazard to Aviation. Nat. Academy Press, 1983.

3. Joppa, Robert G.: Wind Shear Detection Using Measurement of Aircraft Total Energy Change. NASA CR-137839, 1976.

4. Gera, Joseph: Longitudinal Stability and Control in Wind Shear With Energy Height Rate Feedback. NASA TM-81828, 1980.

5. Nicks, Oran W.: A Simple Total Energy Sensor. Soaring, vol. 40, no. 9, Sept. 1976, pp. 30-32.

6. Nicks, Oran W.: How To Make a Total Energy Sensor. Soaring, vol. 41, no. 3, Mar. 1977, pp. 23-24.

7. Nicks, Oran W.: A Simple Total Energy Sensor. NASA TM X-73928, 1976.

8. Nicks, Oran W.: Aircraft Total Energy Sensor. U.S. Pat. 4,061,128, Dec. 6, 1977.

9. Nicks, Oran W.: Further Developments in Simple Total Energy Sensors. Science and Technology of Low Speed and Motorless Flight, Perry W. Hanson, compiler, NASA CP-2085, Part I, 1979, pp. 219-245.

10. Ostroff, Aaron J.; Hueschen, Richard M.; Hellbaum, R. F.; and Creedon, J. F.: Flight Evaluation of a Simple Total Energy-Rate System With Potential Wind-Shear Application. NASA TP-1854, 1981.

11. Ostroff, Aaron J.; Hueschen, Richard M.; Hellbaum, R. F.; Belcastro, Christine M.; and Creedon, J. F.: Evaluation of a Total Energy-Rate Sensor on a Transport Airplane. NASA TP-2212, Nov. 1983.

12. Broussard, John R.: Design, Implementation and Flight Testing of PIF Autopilots for General Aviation Aircraft. NASA CR-3709, 1983.

13. Halyo, Nesim; and Broussard, John R.: Investigation, Development, and Application of Optimal Output Feedback Theory. Volume I - A Convergent Algorithm for the Stochastic Infinite-Time Discrete Optimal Output Feedback Problem. NASA CR-3828, 1984.

14. Maybeck, Peter S.: Stochastic Models, Estimation, and Control. Volume 3. Academic Press, 1982.

15. Dieudonne, James E.: Description of a Computer Program and Numerical Technique for Developing Linear Perturbation Models From Nonlinear Systems Simulations. NASA TM-78710, 1978.

16. Nadkarni, Arun A.: Automatic Flare Transition Penetrating Wind Shears. Paper WA10-C, Proceedings of the 1980 Joint Automatic Control Conference, Volume 1, American Automatic Control Council, c.1980.

17. Halyo, Nesim: Development of an Optimal Automatic Control Law and Filter Algorithm for Steep Glideslope Capture and Glideslope Tracking. NASA CR-2720, 1976.

18. Armstrong, Ernest S.: ORACLS - A Design System for Linear Multivariable Control. Marcel Dekker, Inc., c.1980.

19. Mahesh, J. K.; Konar, A. F.; and Ward, M. D.: Interactive Flight Control System Analysis Program. NASA CR-172352, 1984.

20. Frederick, J. M.; and Tisdale, H. F.: Flight Critical Control Laws for the NASA Terminal Configured Vehicle. D6-32669, Boeing Commercial Airplane Co., [1975].

21. Halyo, Nesim: Terminal Area Automatic Navigation, Guidance, and Control Research Using the Microwave Landing System (MLS). Part 5 - Design and Development of a Digital Integrated Automatic Landing System (DIALS) for Steep Final Approach Using Modern Control Techniques. NASA CR-3681, 1983.

22. Dieudonne, James E.: Comments on a Proposed Standard Wind Hazard Environment and Its Use in Real-Time Aircraft Simulations. AIAA Paper 79-0324, Jan. 1979.

A   continuous plant-state matrix

$\bar{A}$ continuous PIF-state matrix

A_z continuous integrator-state matrix

$A_{11}, A_{12}, A_{21}, A_{22}$ feedforward gain matrices

B   continuous plant-control matrix

$\bar{B}$ continuous PIF-control matrix

B_w wind-gust disturbance matrix

$\bar{B}_w$ PIF wind-gust disturbance matrix

B_z integrator-state transmission matrix

c   coefficient for airspeed and ground-speed feedback gains

D_m control observation matrix for command model

E   error vector used in incremental flight equations

E_1 control matrix for incremental flight equations

F   discrete plant-state transition matrix

$\bar{F}$ discrete PIF-state transition matrix

$\bar{F}_{cl}$ discrete closed-loop transition matrix

F_m discrete command-model state transition matrix

G   discrete plant-control matrix

$\bar{G}$ discrete PIF-control matrix

G_m discrete command-model control matrix

$\bar{G}_w$ discrete PIF disturbance matrix

g   acceleration due to gravity, 32.174 ft/sec^2

H $= h_o + h$

$\bar{H}$ PIF-state observation matrix

H_m command-model state observation matrix

H_x, H_u, H_z plant-state, control-state, and integrator-state observation-matrix
                components comprising the column partitions of the total PIF-state
                observation matrix

38

$\bar{H}_X, \bar{H}_U, \bar{H}_Z$	column partitions of $\bar{H}$ corresponding to X, U, and Z states
h	altitude of airplane, positive up, ft
$\dot{h}_c$	desired-altitude-rate command-model input, ft/sec
h_{cg}	altitude of airplane center of gravity, ft
$\dot{h}_e$	specific total energy rate of the airplane, ft/sec
$\dot{h}_{e,f}$	specific total energy-rate state associated with the pneumatic filter of the energy-rate sensor, ft/sec
$\dot{h}_{e,t}$	specific total energy-rate state associated with the rate transducer of the energy-rate sensor, ft/sec
$\dot{h}_{ke}$	specific kinetic energy rate, ft/sec
h_m	command-model altitude, positive up, ft
$\dot{h}_{pe}$	specific potential energy rate, ft/sec
I	identity matrix
i	imaginary number $(\sqrt{-1})$
J	continuous-time cost function
K	optimal-feedback gain matrix
K_e	engine constant relating engine thrust to throttle position, 596 lb/deg
k	sample integer
$\hat{M}$	PIF discrete-cost-function cross-weighting matrix between states and controls
m	mass
N	number of samples in discrete performance index
$\bar{N}$	PIF output-noise vector
P_A	discrete feedforward matrix
P_{XZ}, P_{UZ}, P_{ZZ}	optimal-output feedback solution matrix partitions corresponding to X, U, and Z
Q	aircraft total pitch rate, $q_0 + q$, rad/sec (deg/sec in figures)
$\bar{Q}$	continuous PIF-state-weighting matrix
$\hat{Q}$	discrete-cost-function PIF-state-weighting matrix

Q_X, Q_U, Q_Z subsets of $\bar{Q}$ relating to plant states **X**, control states **U**, or integrator states **Z**

$\hat{R}$ discrete-cost-function PIF control-weighting matrix

$\bar{R}_V$ continuous PIF control-weighting matrix

t time, sec

U $= u_o + u$

U   control position-command state vector

U^* ideal control star trajectory

U_m command-model control vector

U_w $= u_{w,o} + u_w$

U_z horizontal wind-shear gradient, (ft/sec)/ft

u longitudinal body-axis inertial aircraft-velocity component, positive forward, ft/sec

u_o nominal longitudinal body-axis inertial aircraft-velocity component, positive forward, ft/sec

u_w wind-velocity component in the positive longitudinal direction of the body axes, ft/sec

$u_{w,E}$ wind-velocity component in the positive longitudinal direction of the Earth-fixed inertial frame, ft/sec

$u_{w,g}$ wind-gust component in the positive longitudinal direction of the body axes, ft/sec

$u_{w,o}$ nominal wind-velocity component in the positive longitudinal direction of the body axes, ft/sec

$\dot{u}_{w,o}$ nominal wind-shear acceleration component in the positive longitudinal direction of the body axes, ft/sec

$u_{w,\omega}$ small low-pass cutoff frequency for the horizontal-body-axis wind-velocity component, rad/sec

V   control rate-command vector

V_a airspeed, ft/sec

$V_{a,c}$ desired-airspeed command-model input, ft/sec

$V_{a,m}$ command-model airspeed, ft/sec

$V_{a,x}$ longitudinal airspeed component in the positive forward direction, ft/sec

$\dot{V}_{a,x}$	longitudinal airspeed-rate component in the positive forward direction, ft/sec^2
V_g	ground speed, ft/sec
V_ℓ	ground-speed lower limit for the airspeed-ground-speed implementation, ft/sec
$\bar{V}_m$	measurement-noise covariance matrix
$\bar{V}_p$	control-input process-noise covariance matrix
$\mathbf{V_w}$	wind-velocity vector
W	$= w_o + w$
$\mathbf{W}$	wind-gust and integrator-noise vector
$\bar{W}$	total discrete plant-process-noise covariance matrix
$\bar{W}_g$	plant-process-noise covariance matrix for random wind-gust disturbances
W_w	$= w_{w,o} + w_w$
W_z	vertical wind-shear gradient, (ft/sec)/ft
w	vertical-body-axis inertial aircraft-velocity component, positive down, ft/sec
w_o	nominal aircraft inertial velocity component in the positive vertical direction of the body axes, ft/sec
w_w	wind-velocity component in the positive vertical direction of the body axes, ft/sec
$w_{w,E}$	wind-velocity component in the positive vertical direction of the Earth-fixed inertial frame, ft/sec
$w_{w,g}$	wind-gust component in the positive vertical direction of the body axes, ft/sec
$w_{w,o}$	nominal wind-gust component in the positive vertical direction of the body axes, ft/sec
$\dot{w}_{w,o}$	nominal wind-acceleration component in the positive vertical direction of the body axes, ft/sec^2
$w_{w,\omega}$	small low-pass cutoff frequency for the vertical-body-axis wind-velocity component, rad/sec
X	plant-state vector
$\bar{X}$	PIF-state vector
x^*	ideal state star trajectory

X_f	pneumatic filter state
$\bar{X}_i$	initial-condition error covariance matrix
$\mathbf{X}_m$	command-model state vector
X_t	rate transducer state
X_{th}	throttle-dynamics filter state
x_{cg}	along-track (longitudinal) position of aircraft center of gravity, ft
$\bar{\mathbf{x}}_i$	initial-condition error vector
$\bar{\mathbf{Y}}$	PIF output vector
$\mathbf{Y}_m$	command-model output vector
$\mathbf{Y}_U$	control-state output vector
$\mathbf{Y}_X$	plant-state output vector
$\mathbf{Y}_Z$	integrator-state output vector
$\mathbf{z}$	integrator-state vector
Z_E	aircraft altitude, positive down (i.e., $-H$), ft
α	aerodynamic angle of attack, deg
γ	flight-path angle, deg
Δ	perturbation, deviation, or error
ΔT	discrete sampling period, sec
δ_e	elevator control, deg
δ_{ij}	Kronecker delta
δ_{th}	throttle control, deg
θ	aircraft total pitch attitude, $\theta_o + \theta$, rad (deg for plots)
ω_e	low-pass-filter cutoff frequency associated with the first-order engine lag dynamic model, rad/sec
ω_f	low-pass-filter cutoff frequency for the pneumatic filter associated with the energy-rate sensor, rad/sec
ω_t	low-pass-filter cutoff frequency for the rate transducer associated with the energy-rate sensor, rad/sec

Subscripts:

b	body-axis reference frame
E	Earth-fixed reference frame
k	present time increment
k-1	last time increment
k+1	next time increment
o	nominal
T	total

Superscripts:

T	transpose
-1	inverse
*	ideal star trajectory

Special notation:

E{ }	expectation operator
↑DD	increasing downdraft
↑HW	increasing headwind
↑TW	increasing tailwind
↑UD	increasing updraft

Abbreviations:

c.g.	center of gravity
DR	damping ratio
GM	gain margin
MAC	mean aerodynamic chord
PM	phase margin

A dot over a symbol indicates a first derivative with respect to time. Double dots over a symbol indicate a second derivative with respect to time.

TABLE I.- TSRV B-737 TRIM CONDITIONS

[Landing gear down]

Aircraft parameters	Trim values
Weight, lb	80 000
c.g., percent MAC	25
Flaps, deg	40
Glide slope, deg	3
V_a, knots	125

TABLE II.- CONTINUOUS WEIGHTING AND UNCERTAINTY VALUES

Variable	Trim	Maximum perturbation	Weighting	Uncertainty
States:				
u, ft/sec	211	50	0.0004	10
w, ft/sec	5	10	.01	30
q, rad/sec	0	.02	2 500	.10
θ, rad	-.03	.01	10 000	.20
u_w, ft/sec	0	50	.0004	10
$\dot{w}_w$, ft/sec	0	30	.0011	5
$\dot{h}_{e,f}$, ft/sec	-11	15	.0044	5
$\dot{h}_{e,t}$, ft/sec	-11	15	.0044	5
x_{th}, deg	18.5	5	.04	4
h, ft	1300	2	.25	30
δ_e, deg	2.6	5	.04	2
δ_{th}, deg	18.5	5	.04	5
$\int h$, ft-sec	0	10	.01	0
$\int V_a$, ft	0	12	.007	0
Controls:				
$\dot{\delta}_e$, deg/sec	0	5	0.04	2
$\dot{\delta}_{th}$, deg/sec	0	3	.11	2
Wind:				
$u_{w,g}$, ft/sec	0			60
$w_{w,g}$, ft/sec	0			40
Outputs:				
V_a, ft/sec	211			2.5
q, rad/sec	0			.00035
θ, rad	-.03			.004
h, ft	1300			3
$\dot{h}$, ft/sec	-11			1
$\dot{h}_{e,t}$, ft/sec	-11			1
δ_e, deg	2.6			.01
δ_{th}, deg	18.5			.01
$\int h$, ft-sec	0			.01
$\int V_a$, ft	0			.01

TABLE III.- FEEDBACK GAINS FOR THE DESIGN WITH ENERGY-RATE FEEDBACK

Inputs	Feedback gain for output -									
	V_a	q	θ	h	$\dot{h}$	$\dot{h}_{e,t}$	δ_e	δ_{th}	$\int h$	$\int V_a$
$\dot{\delta}_e$	1.73	507	701	3.37	4.39	0.315	-4.87	0.987	0.488	-0.0093
$\dot{\delta}_{th}$	-2.00	-9.52	-35.5	-.441	-.397	-.191	.0828	-1.52	-.0451	-.250

TABLE IV.- OPEN-LOOP PHUGOID AND SHORT-PERIOD POLES

$$\left[\begin{array}{c} \text{Based on SRI International wind-shear-gradient estimations} \\ \text{for Kennedy airport} \end{array} \right]$$

Wind shear	Phugoid pole	Short-period pole
U_z = 0.25 (ft/sec)/ft, ↑HW; W_z = 0.47 (ft/sec)/ft, ↑UD	0.0140 ± i.271; DR = 0.0517	-0.591 ± i1.17; DR = 0.450
U_z = 0.39 (ft/sec)/ft, ↑TW; W_z = 0.33 (ft/sec)/ft, ↑DD	-0.129 ± i.0843; DR = 0.838	-0.690 ± i.909; DR = 0.604
U_z = 0.39 (ft/sec)/ft, ↑TW; W_z = 0.19 (ft/sec)/ft, ↑UD	0.104 ± i.108; DR = 0.694	-0.620 ± i1.06; DR = 0.505

46

TABLE V.- ANALYSIS RESULTS OF ENERGY-RATE-FEEDBACK CONTROL SYSTEM

Eigenvalue				Frequency response for Bode plot with -		Frequency response of singular value plot for -	
Open loop	DR	Closed loop	DR	δ_e open	δ_{th} open	Additive disturbances	Multiplicative disturbances
Design case ($U_z = 0$; $W_z = 0$)							
$-0.017 \pm i.164$ $-.649 \pm i1.020$ -2.400 -1.130 $-.750$ 0 0 0 0 0 0	0.101 $.535$	$-0.585 \pm i.599$ $-1.370 \pm i2.080$ $-2.680 \pm i.467$ -1.340 $-.482 \pm i.354$ $-.282$ $-.193 \pm i.154$ 0 0	0.699 $.551$ $.985$ $.805$ $.780$	GM, -12.40 dB PM, $39.20°$	GM, -14.13 dB PM, $47.20°$	GM $\left\{\begin{array}{l}7.20\text{ dB}\\-3.88\text{ dB}\end{array}\right.$ PM, $\pm32.72°$	GM $\left\{\begin{array}{l}4.42\text{ dB}\\-9.48\text{ dB}\end{array}\right.$ PM, $\pm38.80°$
Off-design case ($U_z = 0.39$ (ft/sec)/ft, ↑TW; $W_z = 0.19$ (ft/sec)/ft, ↑UD)							
$0.104 \pm i.108$ $-.620 \pm i1.06$ -2.400 -1.130 $-.750$ $-.299$ 0 0 0 0 0 0	0.694 $.505$	$-0.494 \pm i.907$ $-1.500 \pm i2.170$ $-2.940 \pm i.621$ $-.736 \pm i.512$ $-.351$ $-.202 \pm i.182$ $-.191$ 0 $.020$	0.478 $.567$ $.978$ $.821$ $.743$	GM $\left\{\begin{array}{l}12.23\text{ dB}\\-12.43\text{ dB}\end{array}\right.$ PM, $41.10°$	GM, -10.24 dB PM, $48.80°$	GM $\left\{\begin{array}{l}5.35\text{ dB}\\-3.28\text{ dB}\end{array}\right.$ PM, $\pm26.57°$	GM $\left\{\begin{array}{l}3.38\text{ dB}\\-5.60\text{ dB}\end{array}\right.$ PM, $\pm27.49°$

TABLE VI.- FEEDBACK GAINS FOR THE REDESIGN WITHOUT ENERGY-RATE FEEDBACK

Input	Feedback gain for output -									
	V_a	q	θ	h	$\dot{h}$	$\dot{h}_{e,t}$	δ_e	δ_{th}	$\int h$	$\int V_a$
$\dot{\delta}_e$	1.92	510.0	672.0	3.42	4.46	0	-4.80	1.35	0.478	-0.045
$\dot{\delta}_{th}$	-2.02	-11.6	-19.8	-.45	-.42	0	.05	-1.67	-.041	-.230

TABLE VII.- ANALYSIS RESULTS OF REDESIGNED CONTROL SYSTEM
WITHOUT ENERGY-RATE FEEDBACK

Eigenvalue		Frequency response for Bode plot with -		Frequency response of singular value plot for -	
Closed loop	DR	δ_e open	δ_{th} open	Additive disturbances	Multiplicative disturbances
Design case ($U_z = 0$; $W_z = 0$)					
-0.617 ± i.531	0.758	GM, -12.35 dB	GM, -15.85 dB	GM $\begin{cases} 7.28 \text{ dB} \\ -3.90 \text{ dB} \end{cases}$	GM $\begin{cases} 4.45 \text{ dB} \\ -9.61 \text{ dB} \end{cases}$
-1.460 ± i2.010	.589	PM, 39.50°	PM, 41.60°	PM, ±32.97°	PM, ±39.10°
-2.400					
-1.860 ± i.340	.984				
-1.130					
-.292					
-.202 ± i.278	.587				
-.176					
0					
0					
Off-design case ($U_z = 0.39$ (ft/sec)/ft, ↑TW; $W_z = 0.19$ (ft/sec)/ft, ↑UD)					
-0.374 ± i.447	0.642	GM $\begin{cases} 12.21 \text{ dB} \\ -12.39 \text{ dB} \end{cases}$	GM, -11.38 dB	GM $\begin{cases} 5.16 \text{ dB} \\ -3.21 \text{ dB} \end{cases}$	GM $\begin{cases} 3.44 \text{ dB} \\ -5.77 \text{ dB} \end{cases}$
-1.580 ± i2.020	.617	PM, 40.20°	PM, 43.30°	PM, ±25.87°	PM, ±28.10°
-2.430					
-2.400					
-1.130					
-.958 ± i.861	.744				
-.200 ± i.205	.698				
-.121					
0					
.020					
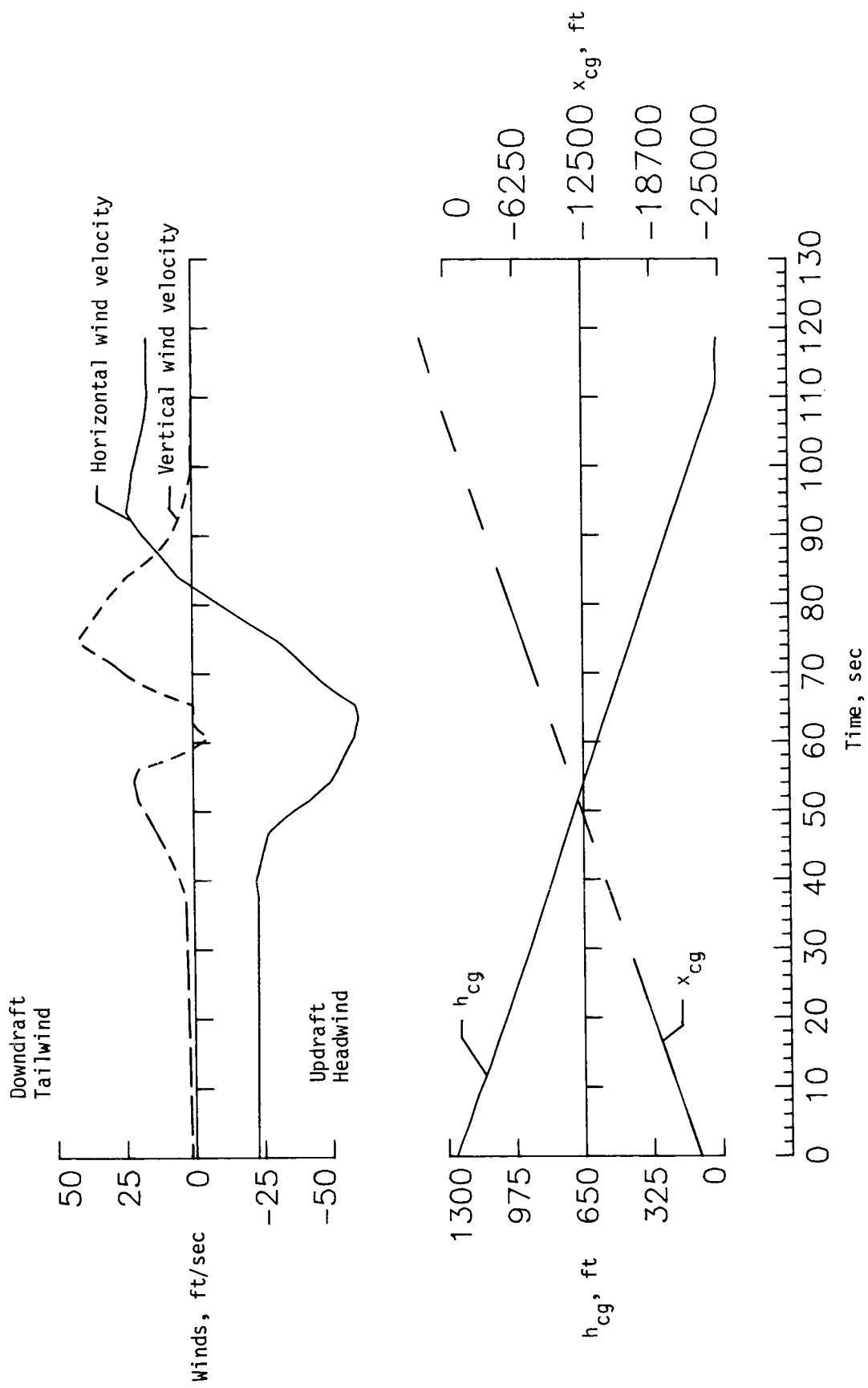
Figure 1.- SRI International Kennedy airport wind-shear environment.
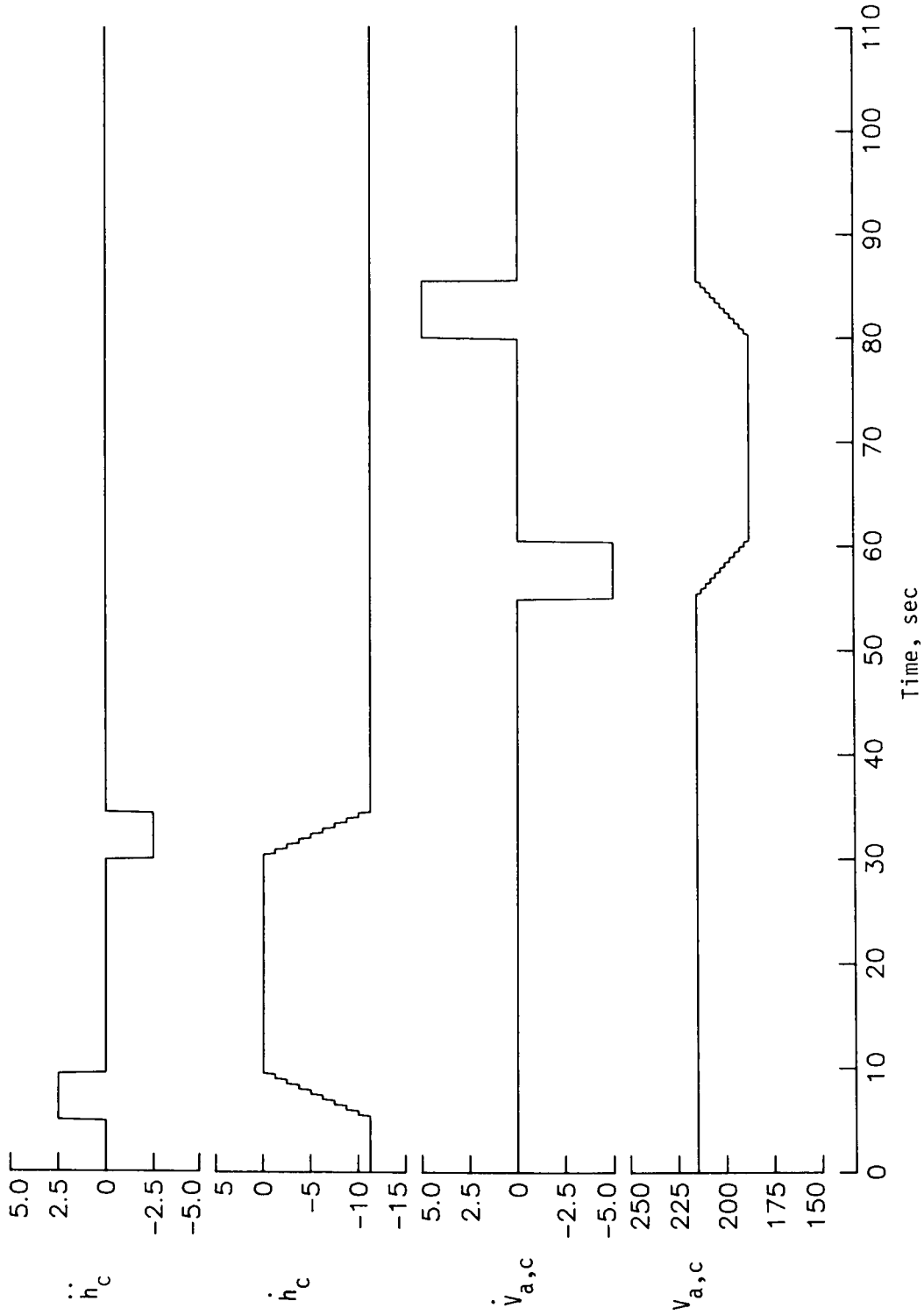
Figure 2.- Command-model inputs.

50
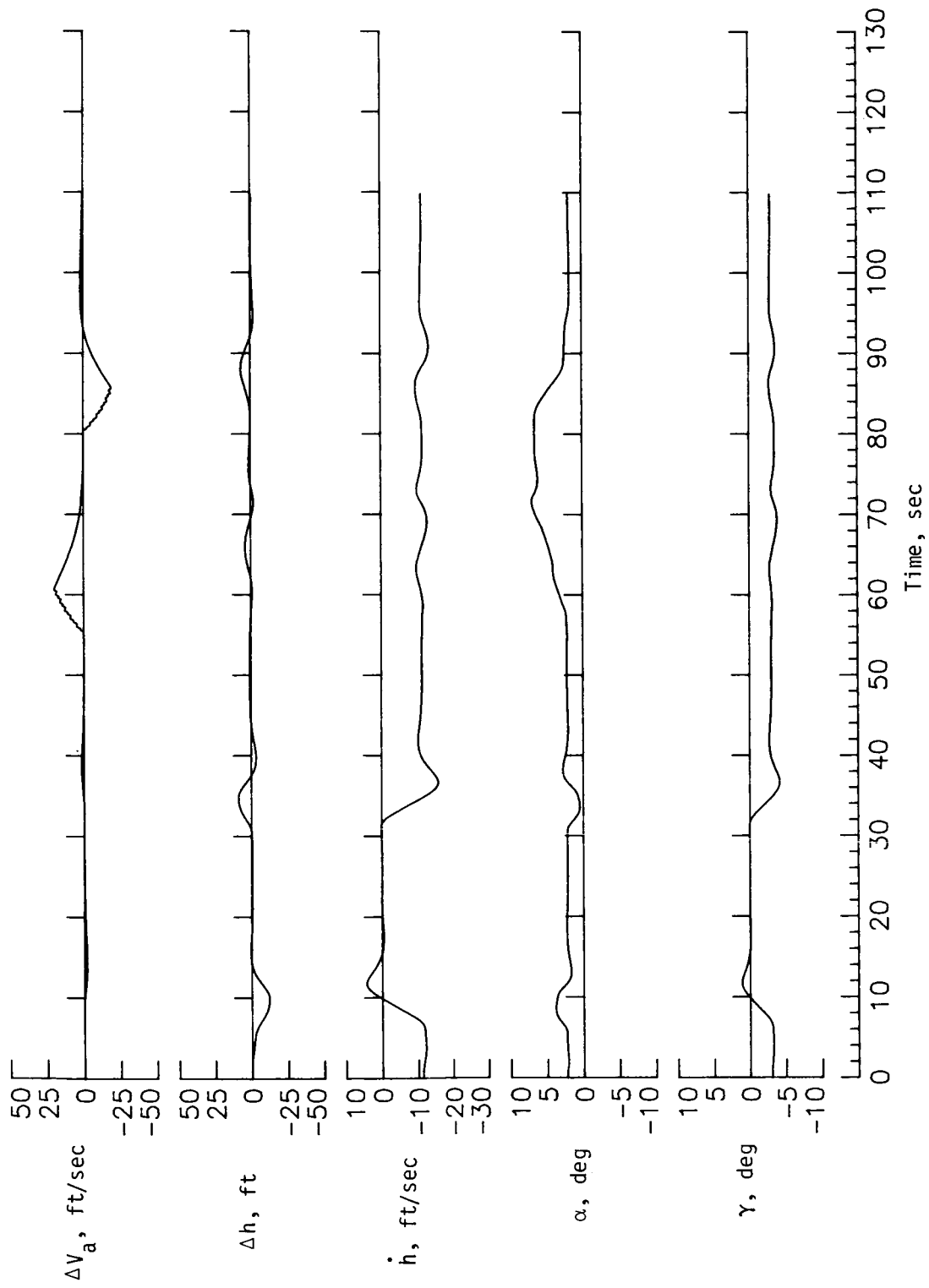
Figure 3.- Command following with the TSRV B-737 radar altimeter.
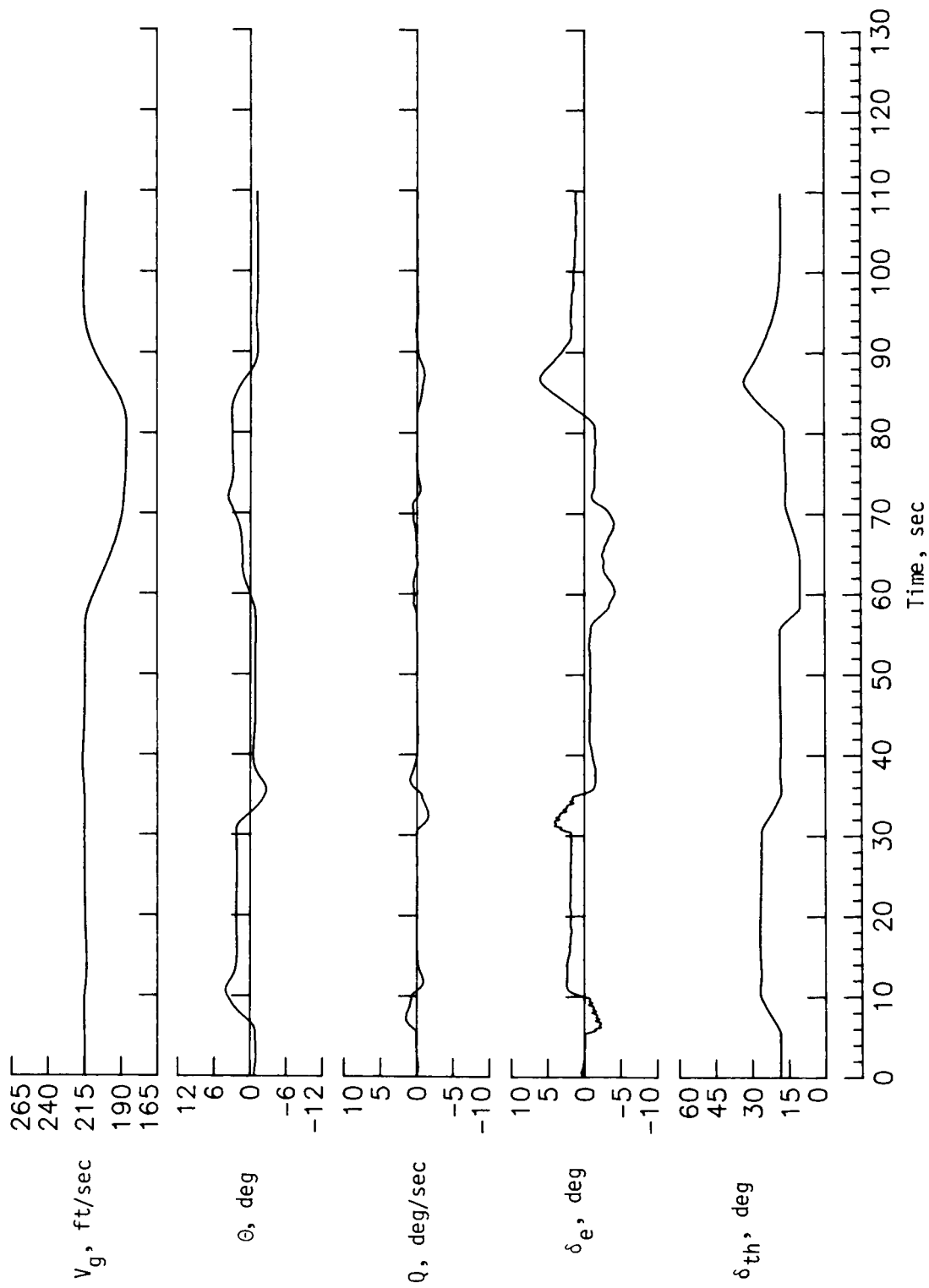
Figure 3.- Concluded.

52
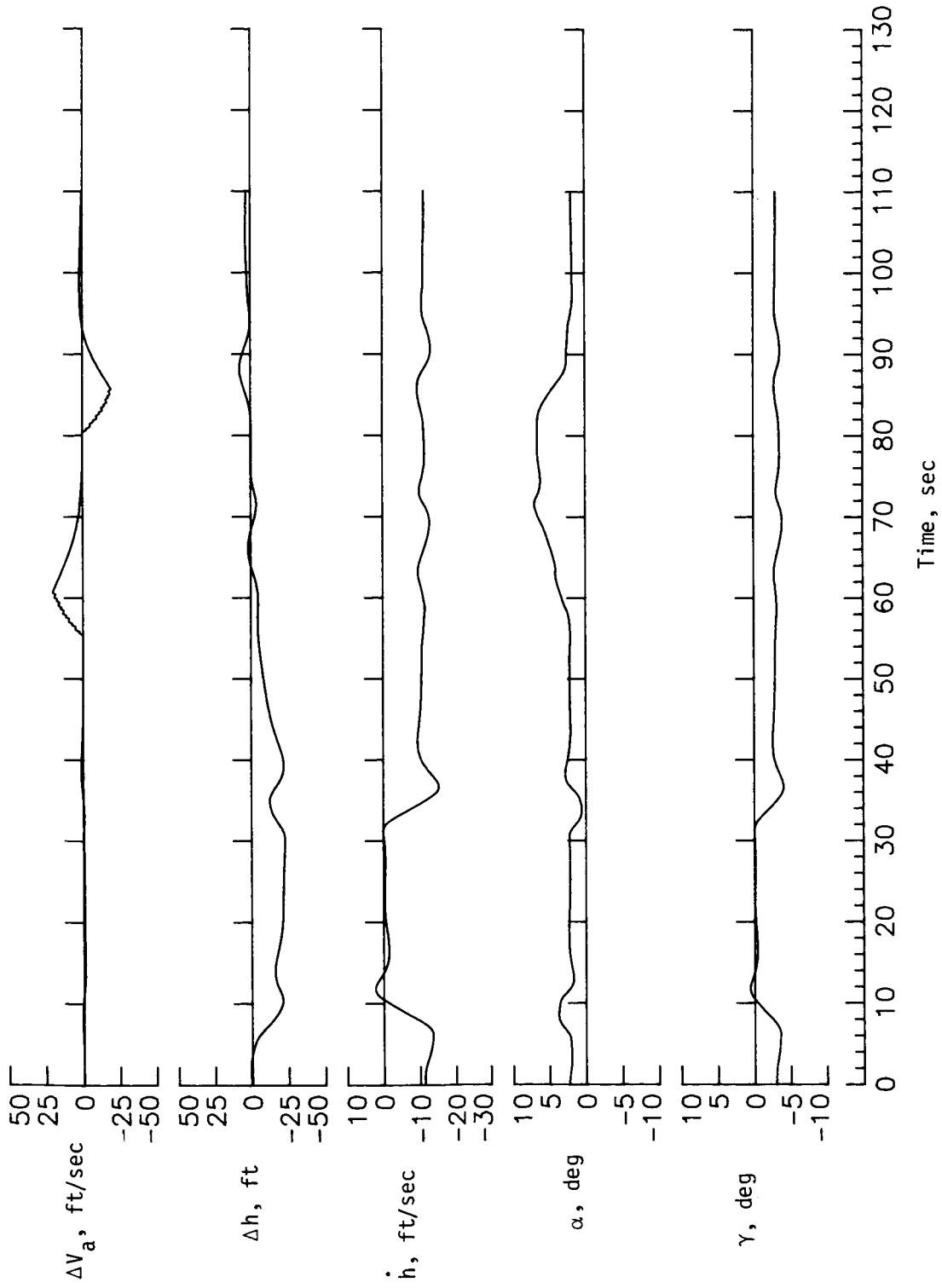
Figure 4.- Command following with estimated altitude from a complementary filter.
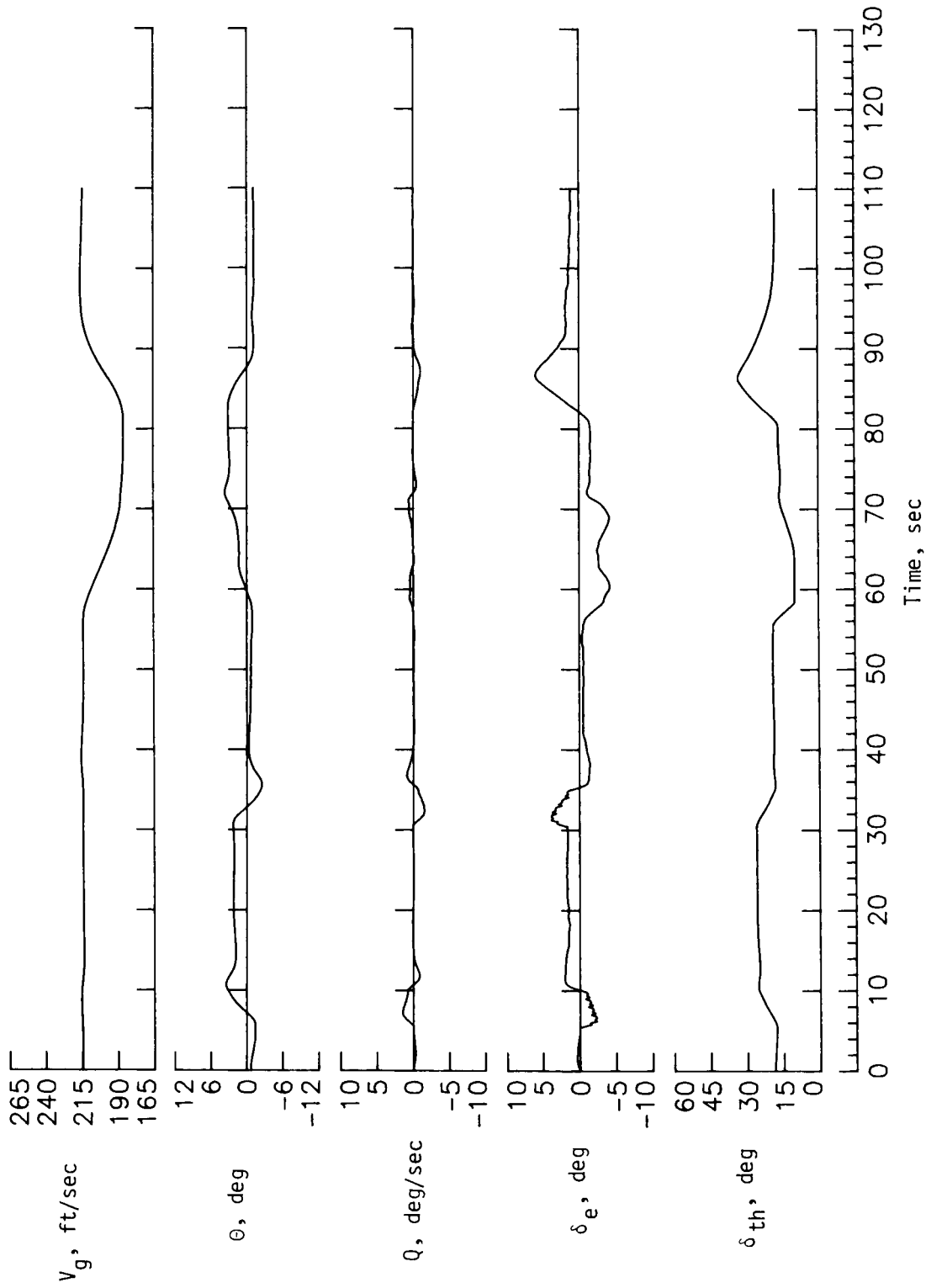
Figure 4.- Concluded.

54
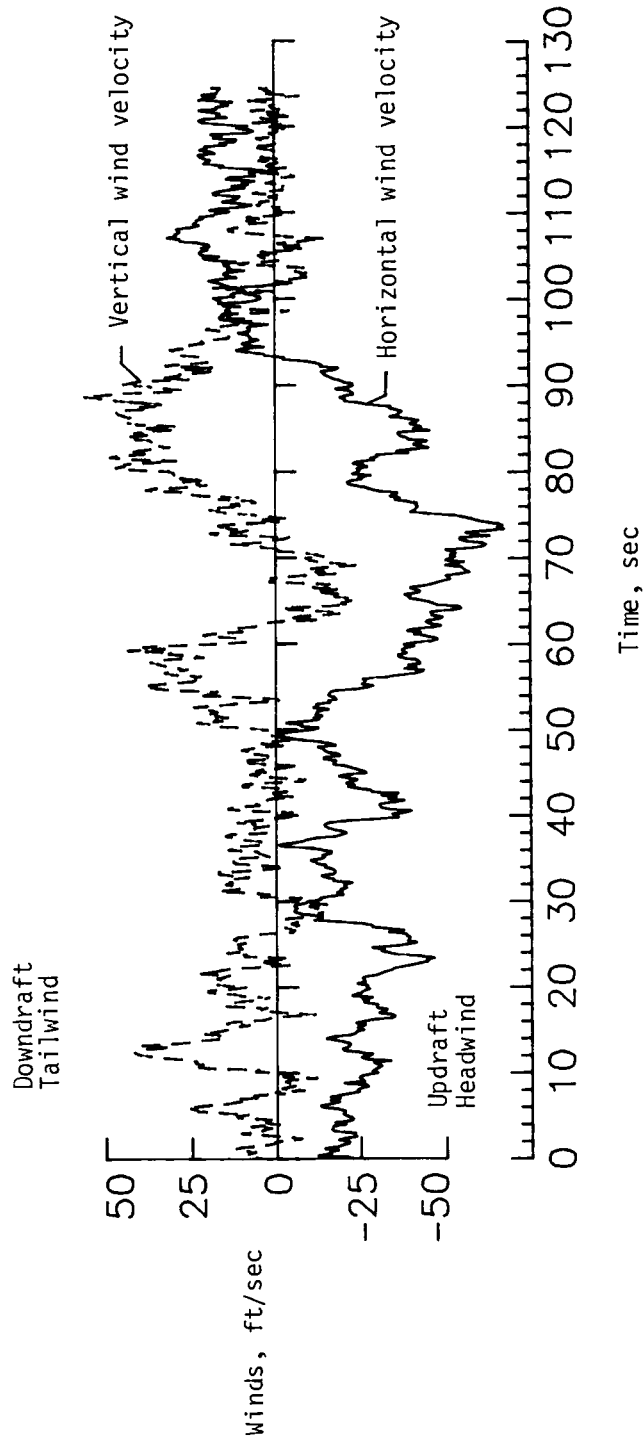
Figure 5.- SRI International Kennedy airport wind-shear environment with gusts.
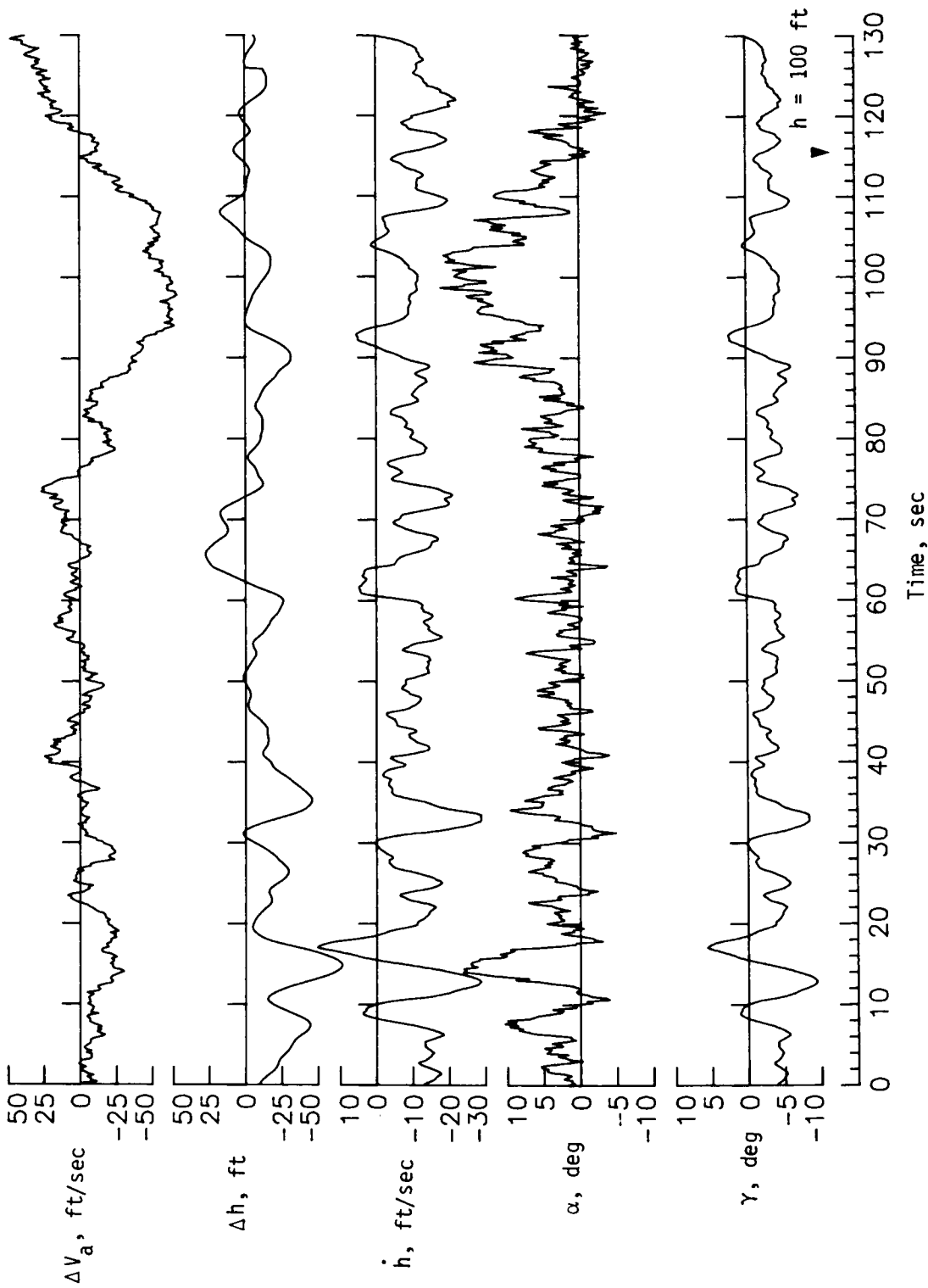
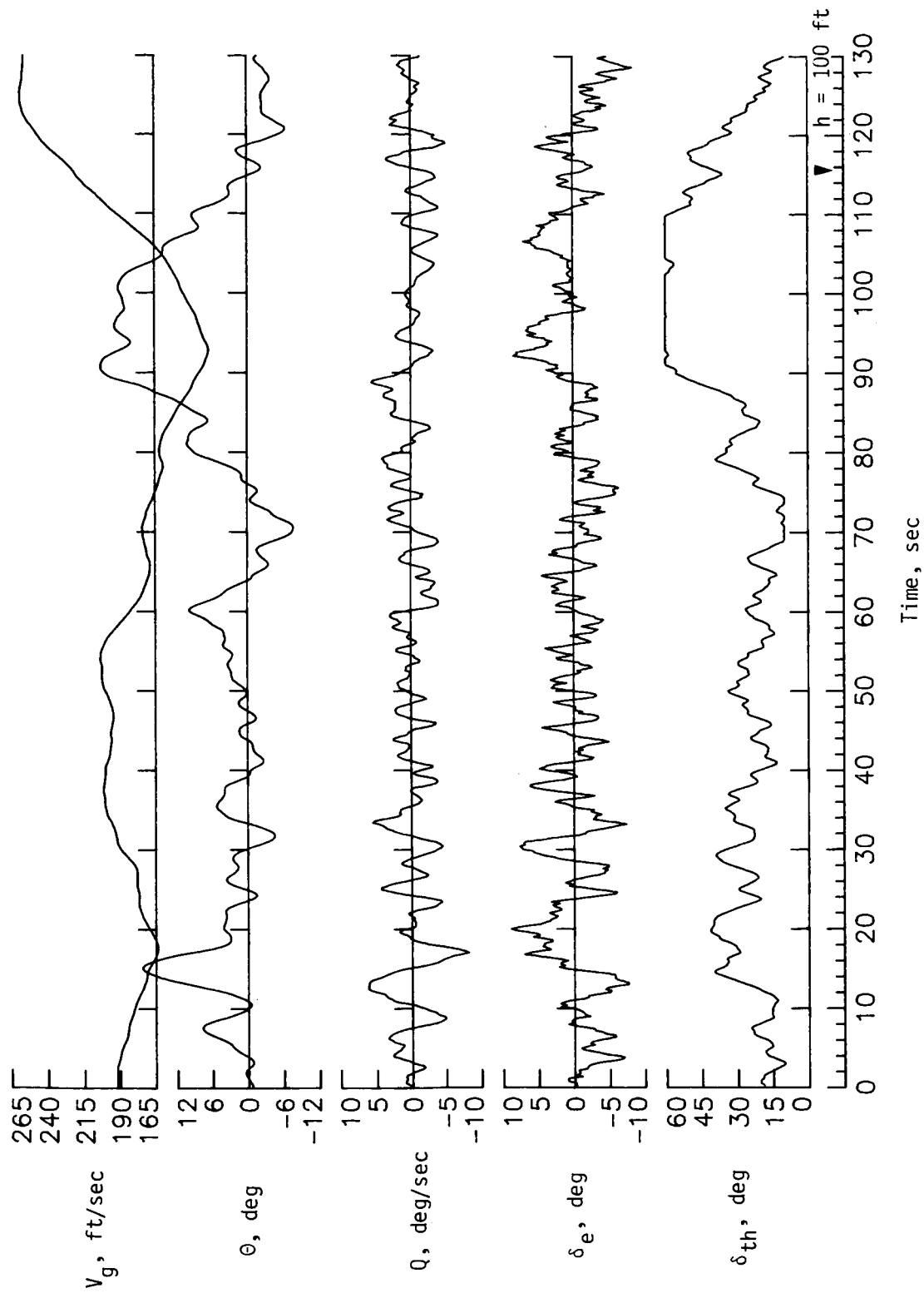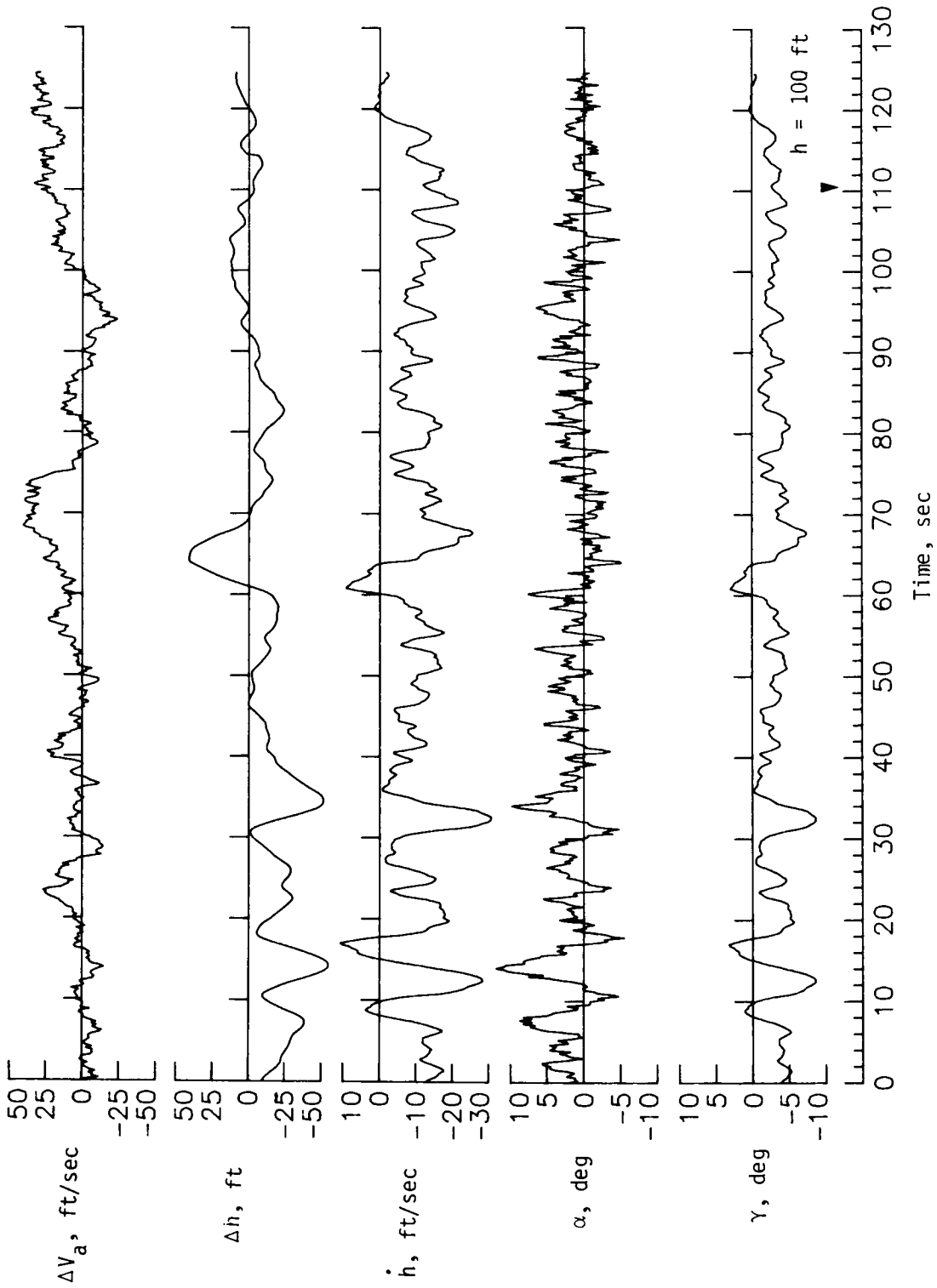Figure 6.- Performance of design with energy-rate feedback and airspeed control.

Figure 6.- Concluded.

Figure 7.- Performance of energy-rate design with airspeed and ground-speed control.

58
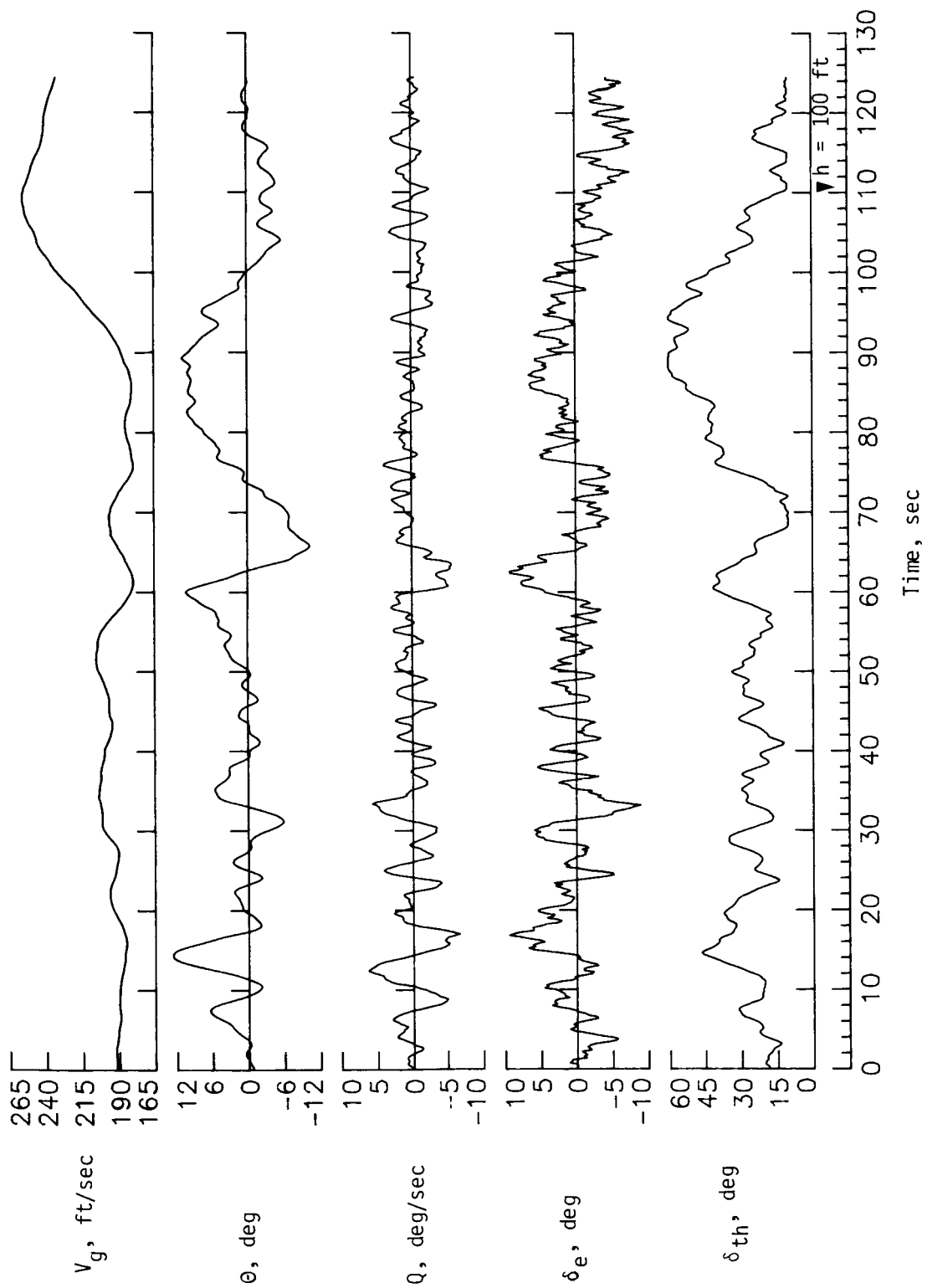
Figure 7.- Concluded.

59
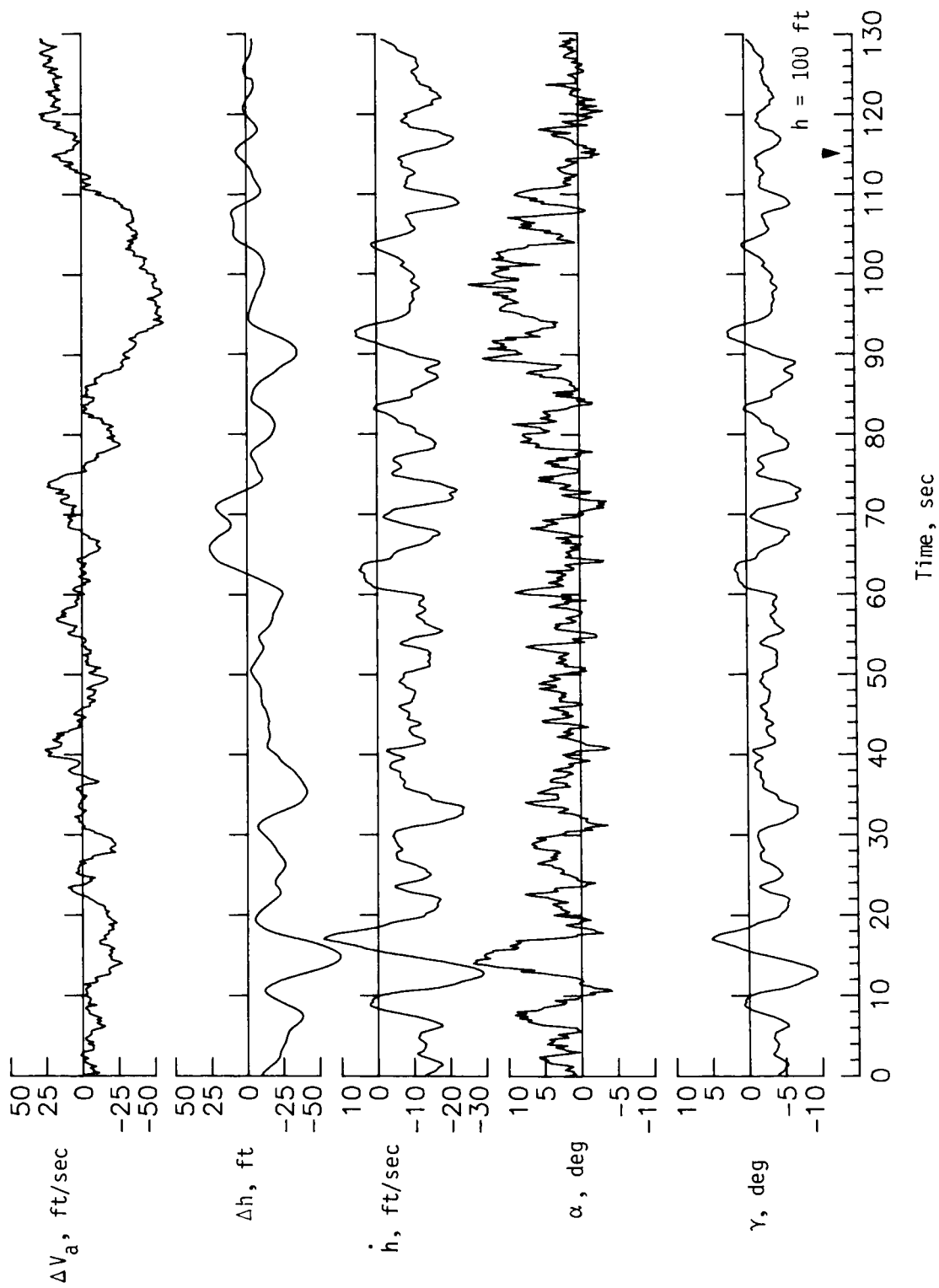
Figure 8.- Performance of redesign without energy-rate feedback and with airspeed control.
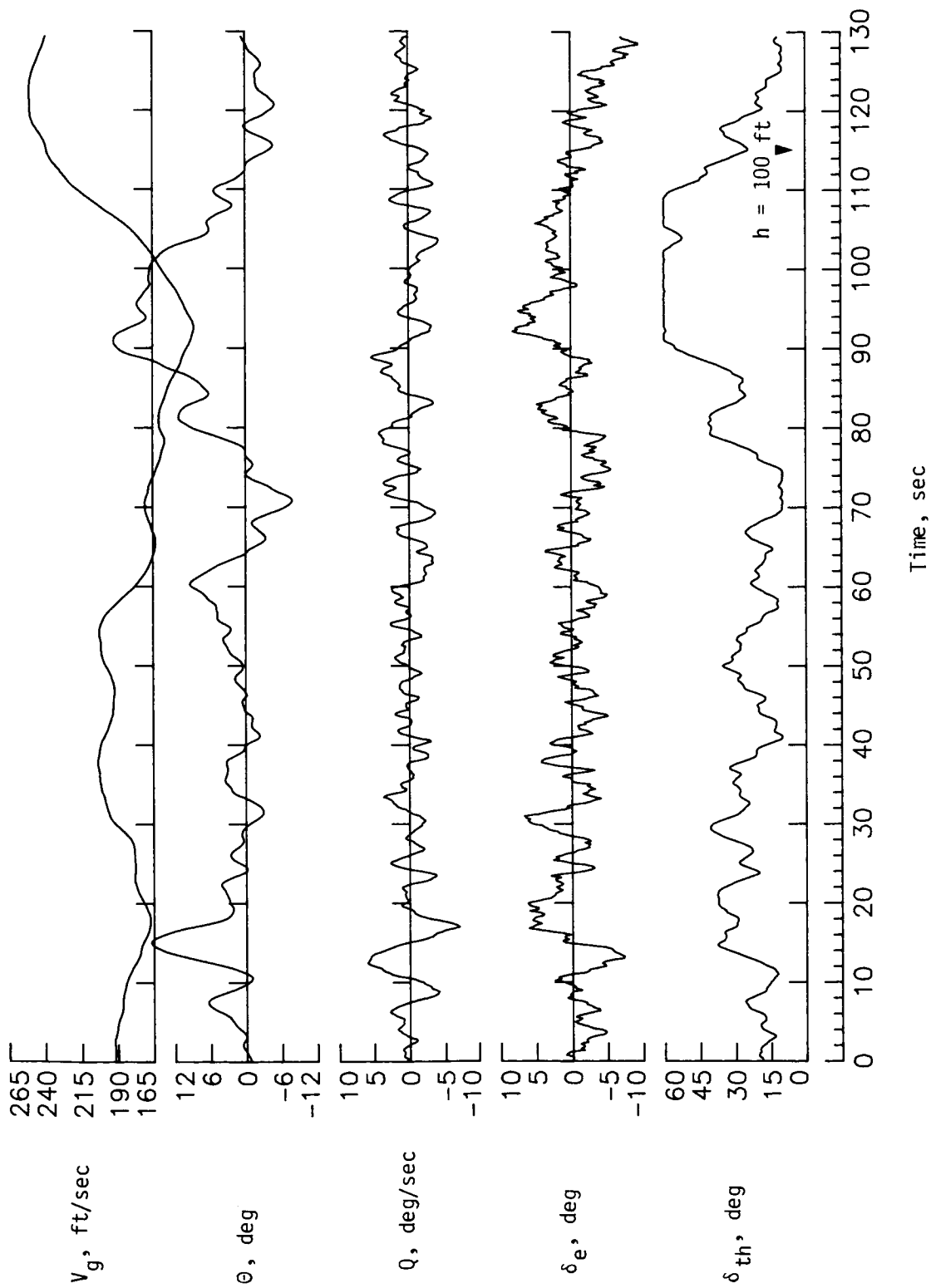
Figure 8.- Concluded.
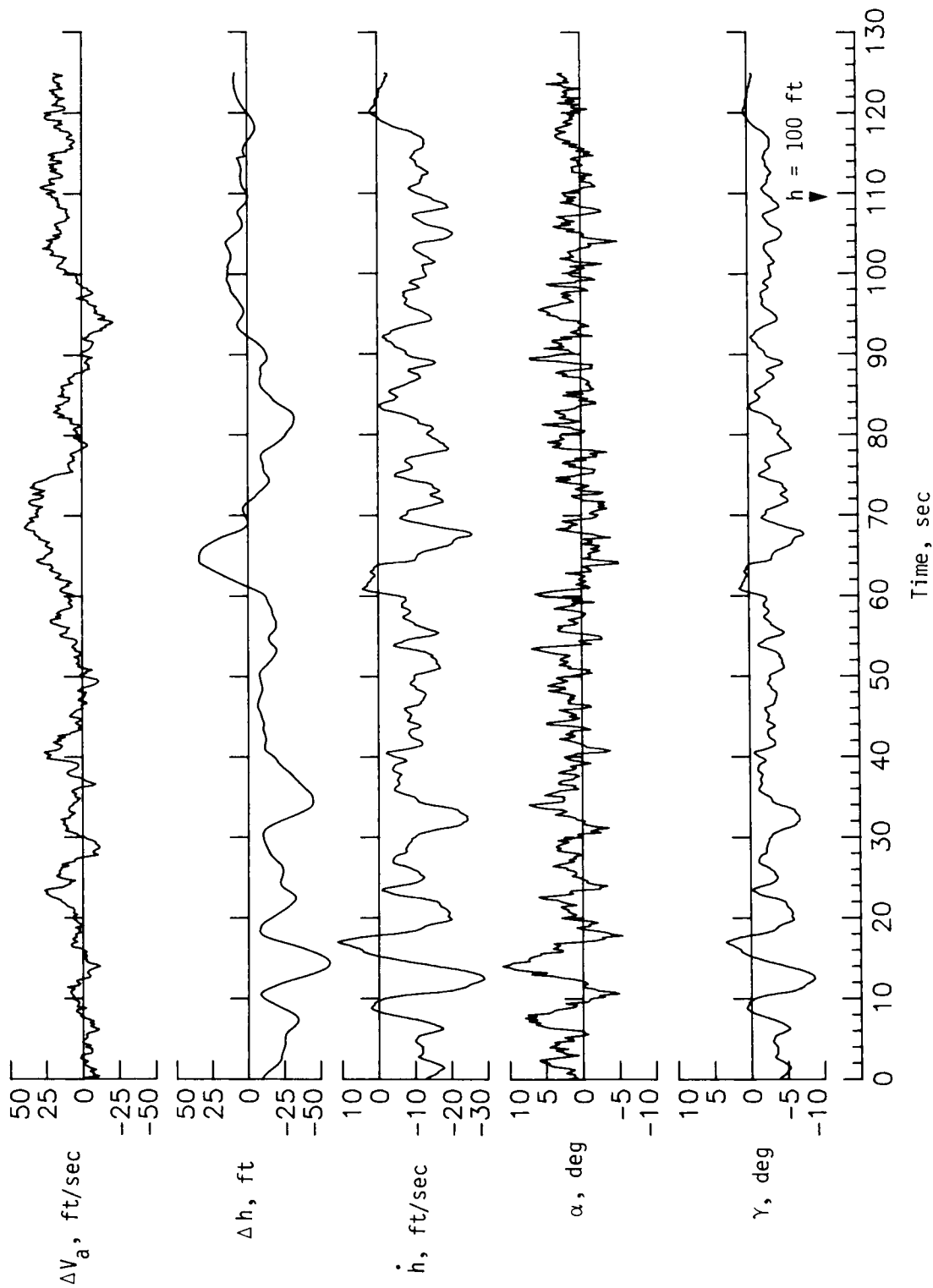
Figure 9.- Performance of redesign without energy-rate feedback and with airspeed and ground-speed control.
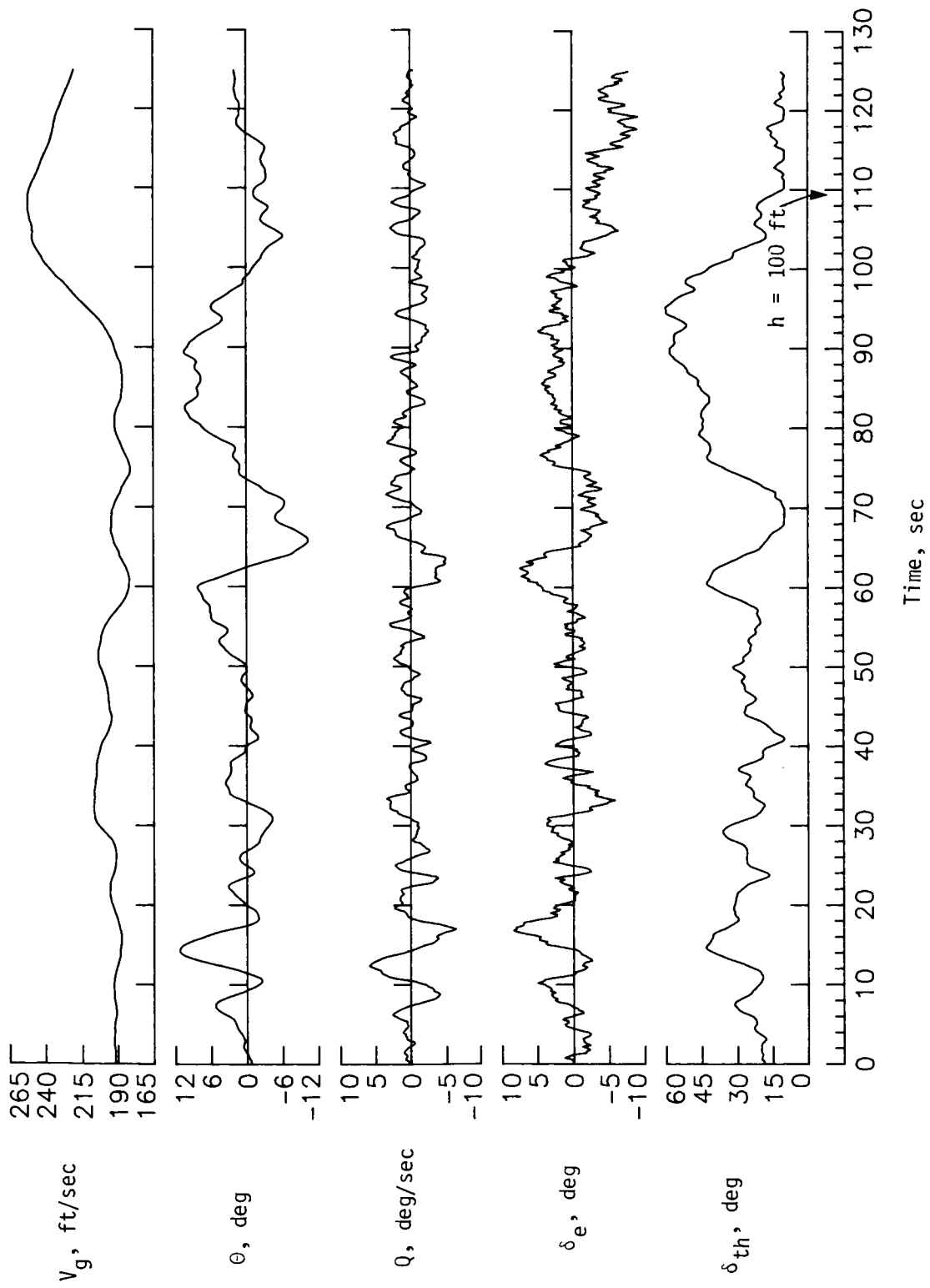
Figure 9.- Concluded.
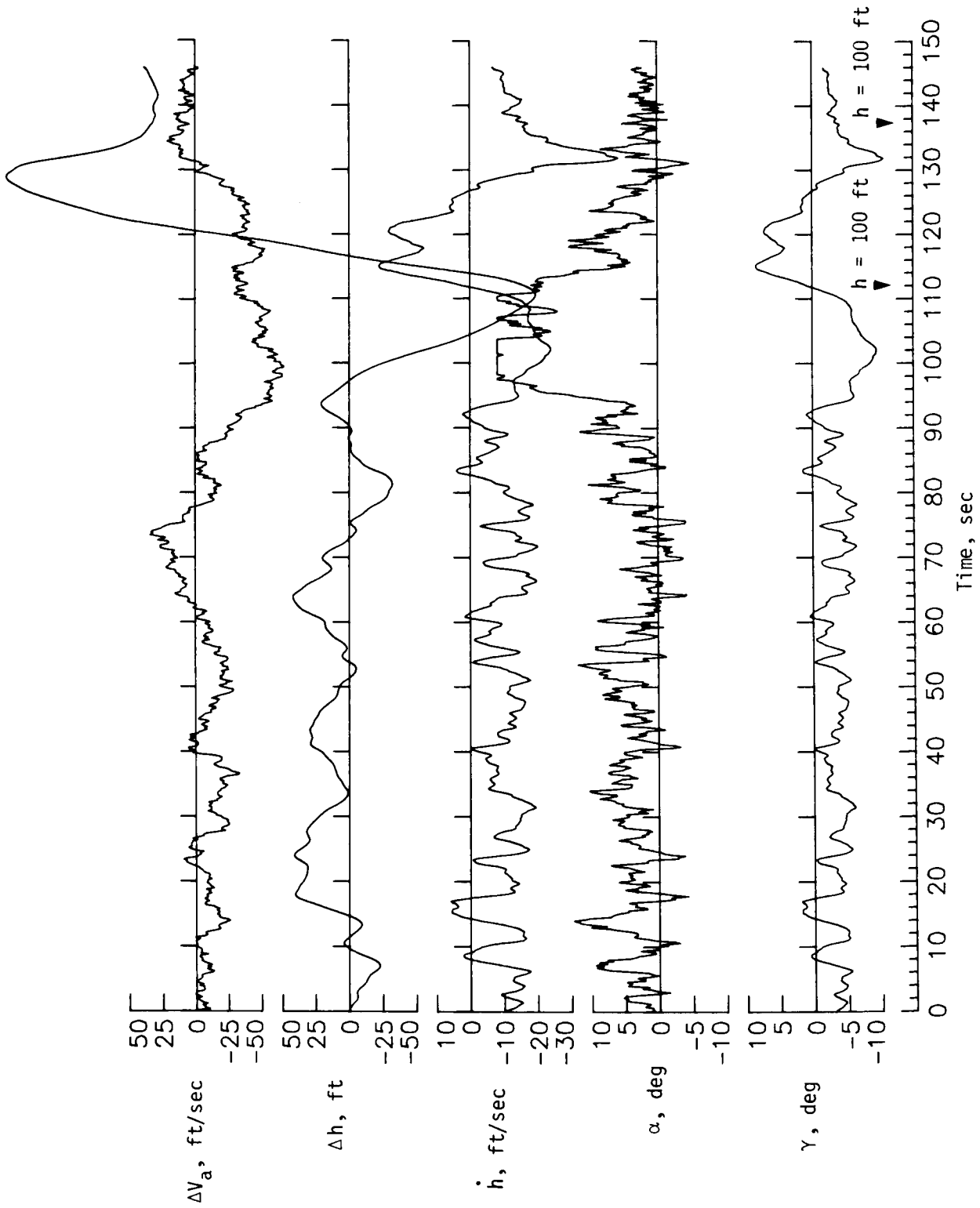
Figure 10.- Performance of TSRV B-737 ILS autoland system.

64
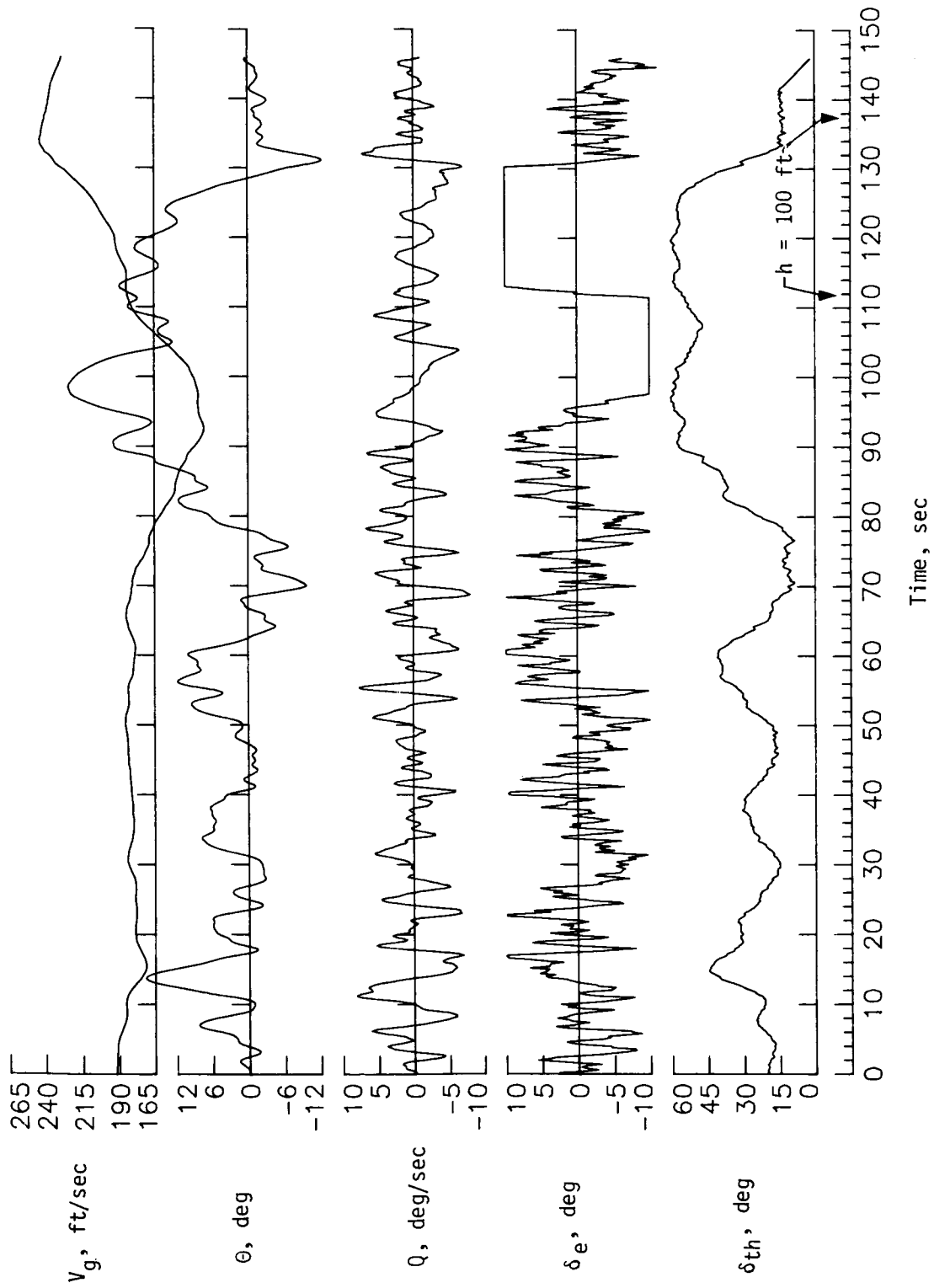
Figure 10.- Concluded.
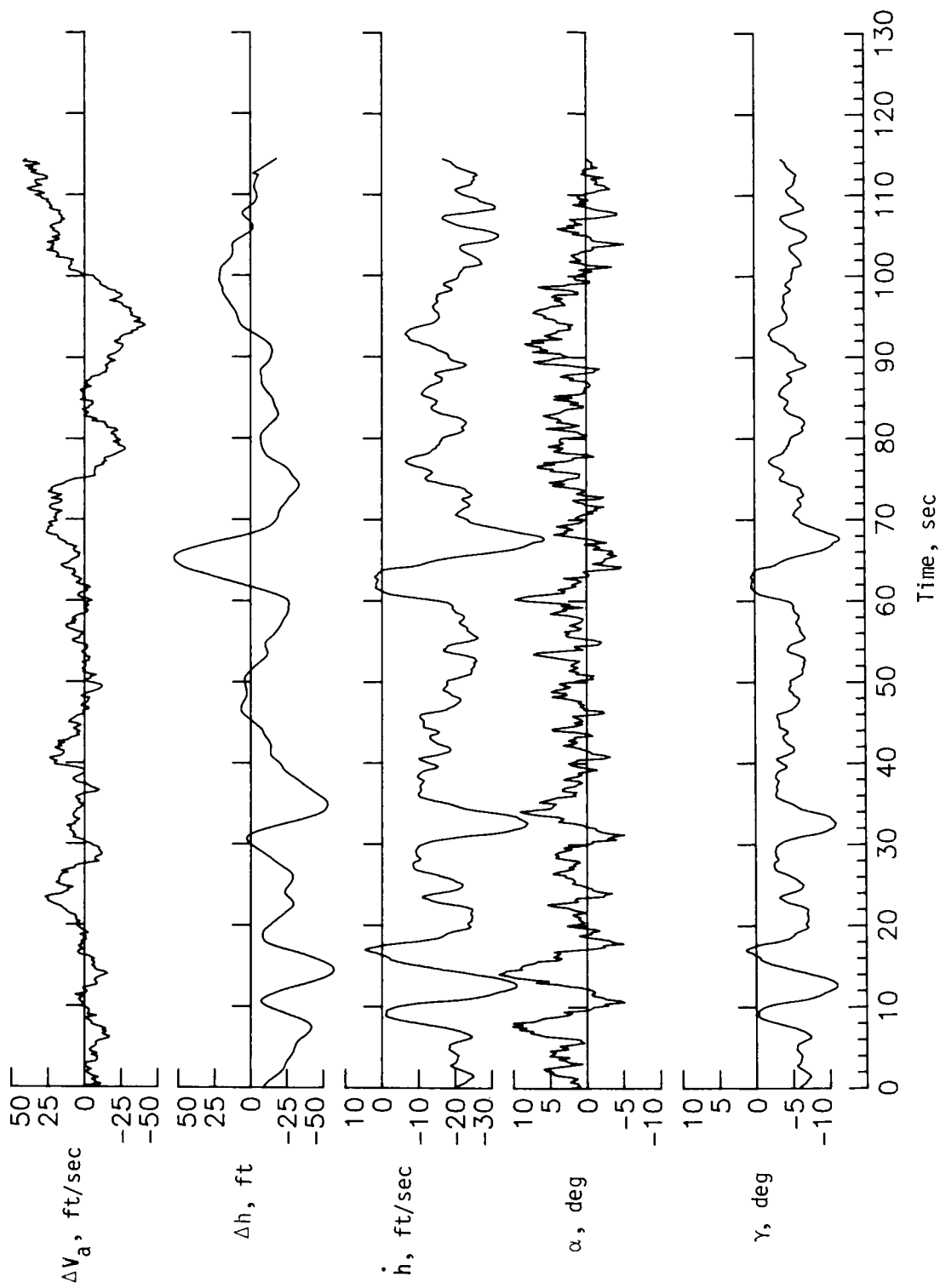
Figure 11.- Energy-rate design with airspeed and ground-speed control for 5° glide slope.
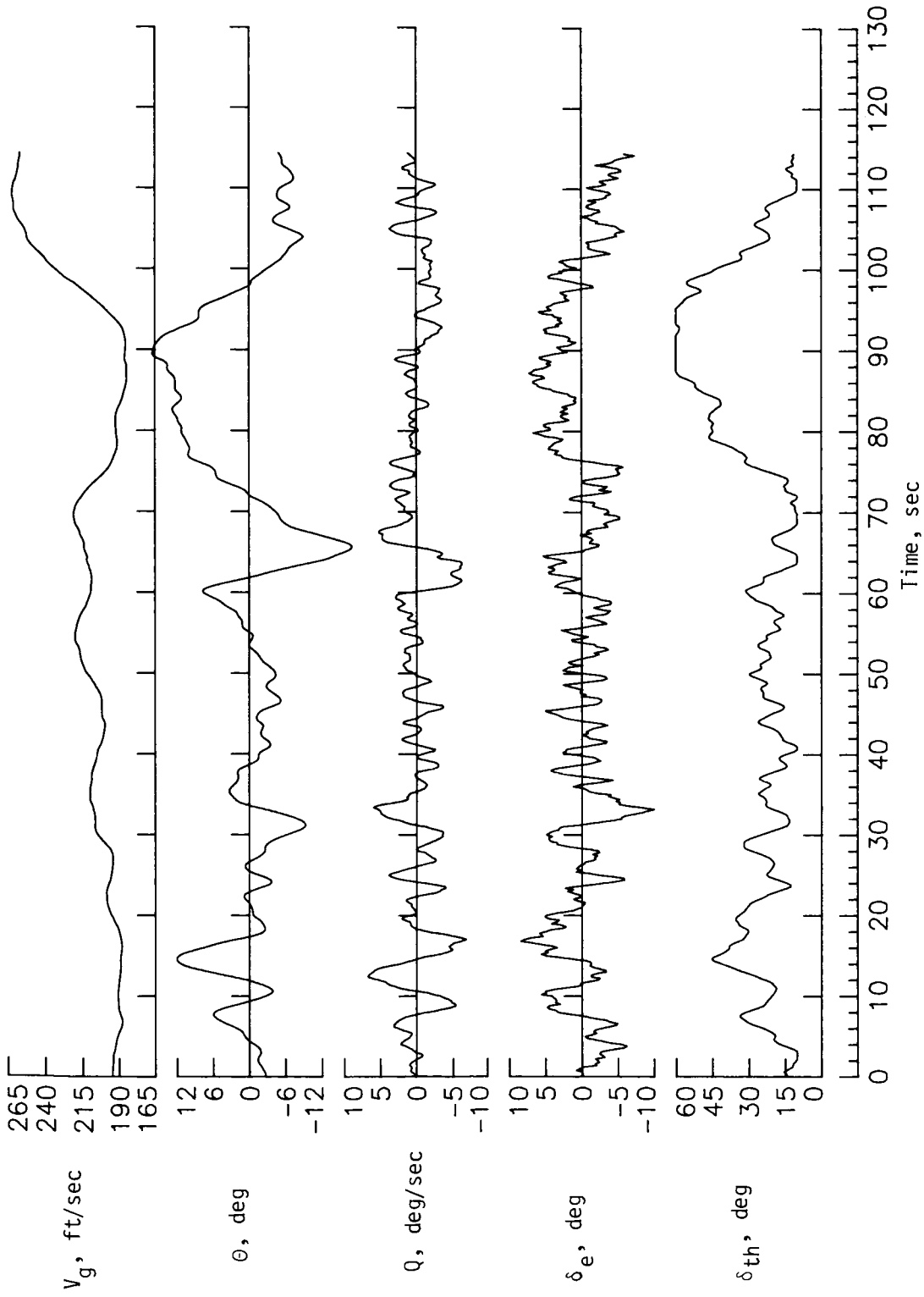
Figure 11.- Concluded.
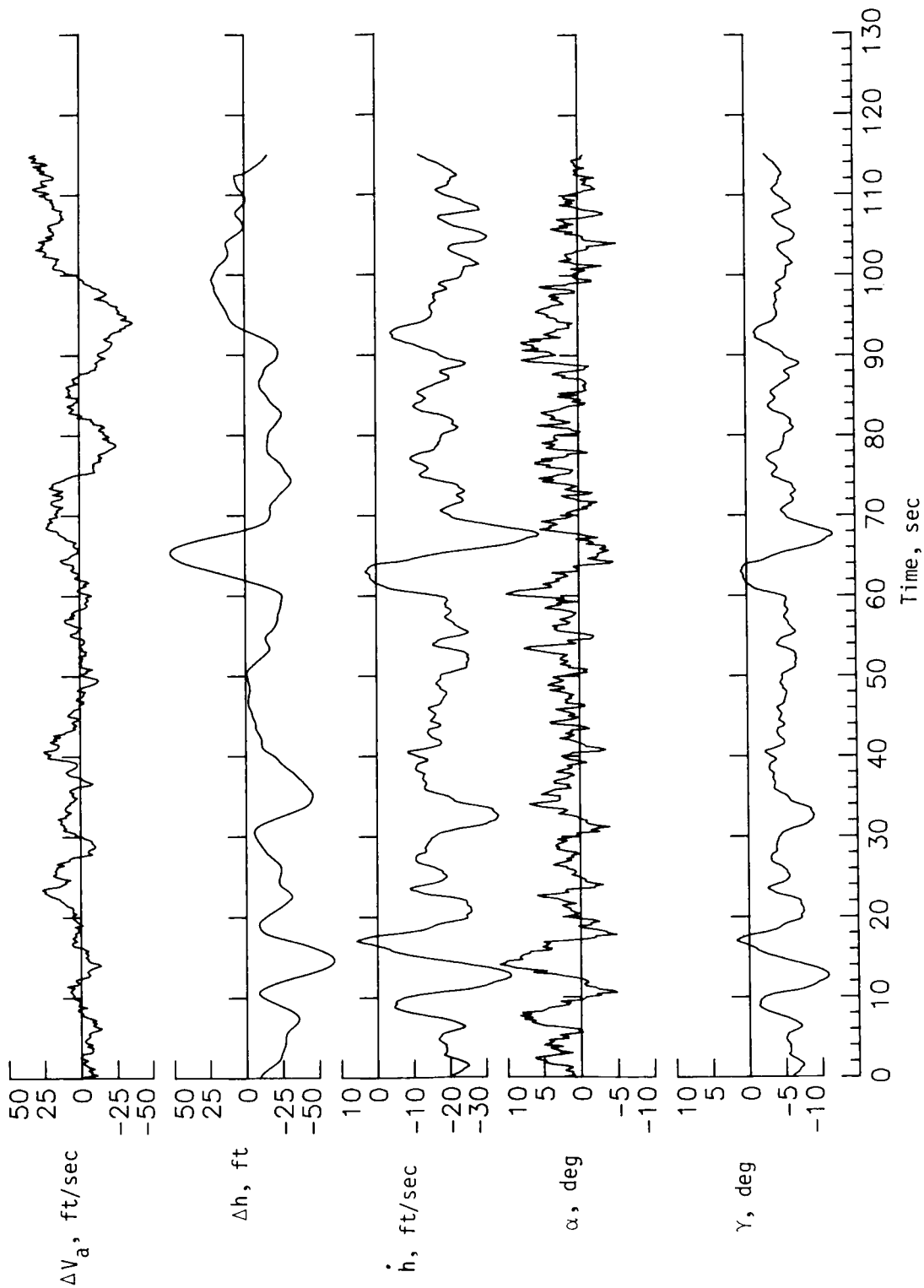
Figure 12.- Redesign with airspeed and ground-speed control for 5° glide slope.
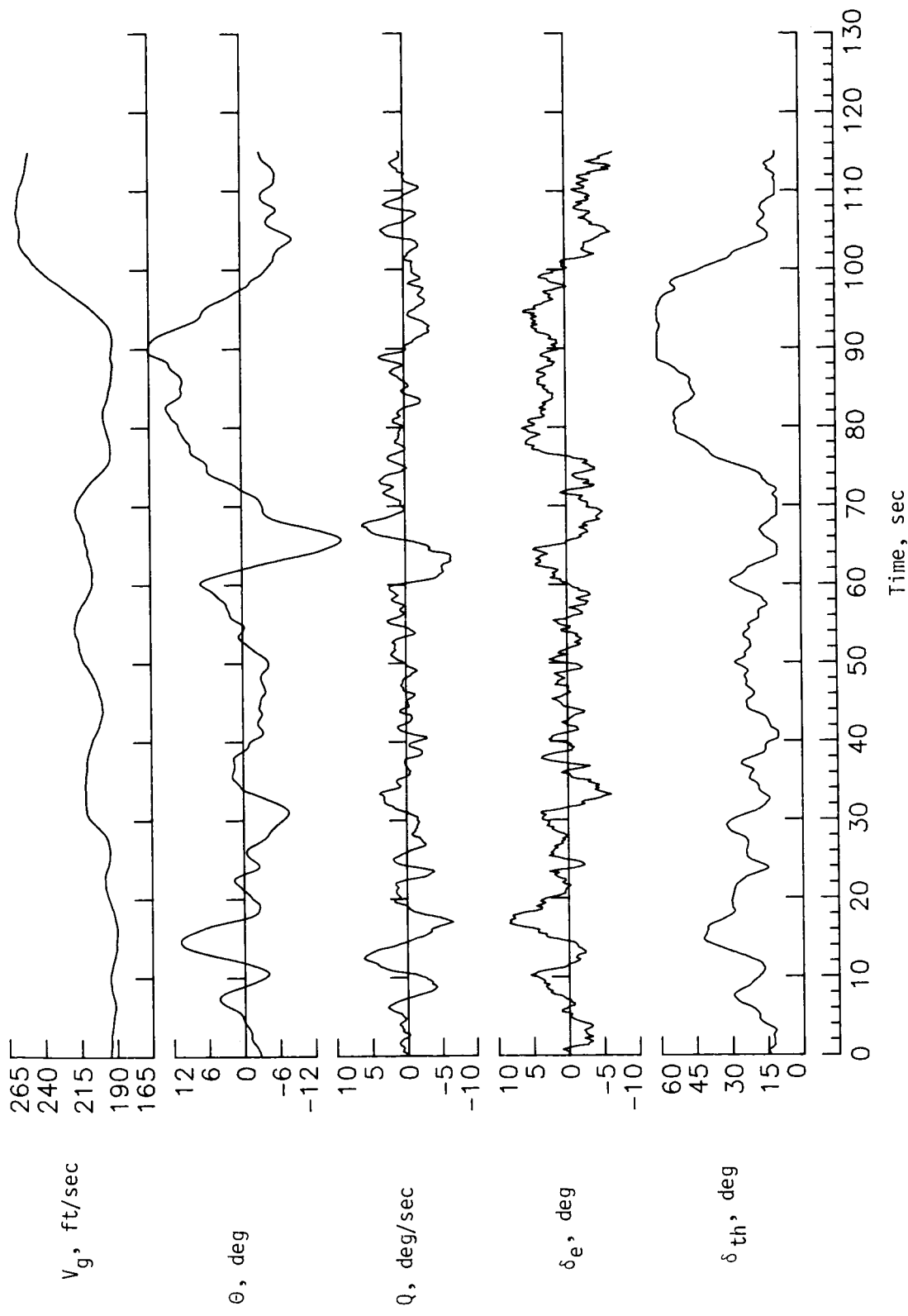
Figure 12.- Concluded.

1. Report No. NASA TP-2412	2. Government Accession No.	3. Recipient's Catalog No.
4. Title and Subtitle TOTAL ENERGY-RATE FEEDBACK FOR AUTOMATIC GLIDE-SLOPE TRACKING DURING WIND-SHEAR PENETRATION		5. Report Date May 1985
		6. Performing Organization Code 505-45-33-04
7. Author(s) Christine M. Belcastro and Aaron J. Ostroff		8. Performing Organization Report No. L-15845
		10. Work Unit No.
9. Performing Organization Name and Address NASA Langley Research Center Hampton, VA 23665		11. Contract or Grant No.
		13. Type of Report and Period Covered Technical Paper
12. Sponsoring Agency Name and Address National Aeronautics and Space Administration Washington, DC 20546		14. Sponsoring Agency Code

15. Supplementary Notes

16. Abstract
Low-altitude wind shear is recognized as an infrequent but significant hazard to all aircraft during the take-off and landing phases of flight. A total energy-rate sensor, which is potentially applicable to this problem, has been developed for measuring the specific total energy rate of an airplane with respect to the air mass. This paper presents control-system designs, both with and without energy-rate feedback, for the approach to landing of a transport airplane through a severe-wind-shear and gust environment in order to evaluate this application of the sensor. A system model is developed which incorporates wind-shear-dynamics equations with the airplane equations of motion, thus allowing the control systems to be analyzed under various wind-shear conditions. The control systems are designed using optimal-output feedback and are analyzed using frequency-domain control-theory techniques. Control-system performance is evaluated using a complete nonlinear simulation of the airplane combined with a severe-wind-shear and gust data package. This evaluation is concerned with control system stability and regulation capability only - operational performance aspects are not considered. The analysis and simulation results indicate very similar stability and performance characteristics for the two designs.

17. Key Words (Suggested by Author(s)) Wind shear Optimal control Output feedback Energy-rate feedback	18. Distribution Statement Unclassified - Unlimited Subject Category 08

19. Security Classif. (of this report) Unclassified	20. Security Classif. (of this page) Unclassified	21. No. of Pages 72	22. Price A04

THIRD-CLASS BULK RATE

NASA